



Article

Dual Emissive Zn(II) Naphthalocyanines: Synthesis, Structural and Photophysical Characterization with Theory-Supported Insights towards Soluble Coordination Compounds with Visible and Near-Infrared Emission

Sidharth Thulaseedharan Nair Sailaja ^{1,2} , Iván Maisuls ^{1,2}, Alexander Hepp ¹ , Dana Brünink ³, Nikos L. Doltsinis ³ , Andreas Faust ^{4,5}, Sven Hermann ^{4,5} and Cristian A. Strassert ^{1,2,*}

- ¹ Institut für Anorganische und Analytische Chemie, Universität Münster, Corrensstraße 28/30, 48149 Münster, Germany; maisuls@uni-muenster.de (I.M.); alexander.hepp@uni-muenster.de (A.H.)
² CeNTech, CiMIC, SoN, Universität Münster, Heisenbergstraße 11, 48149 Münster, Germany
³ Institute for Solid State Theory and Center for Multiscale Theory and Computation, Universität Münster, Wilhelm-Klemm-Straße 10, 48149 Münster, Germany
⁴ European Institute for Molecular Imaging, Universität Münster, Röntgenstraße 16, 48149 Münster, Germany; faustan@uni-muenster.de (A.F.)
⁵ Department of Nuclear Medicine, University Hospital Münster, Albert-Schweitzer-Campus 1, 48149 Münster, Germany
* Correspondence: ca.s@uni-muenster.de



Citation: Sailaja, S.T.N.; Maisuls, I.; Hepp, A.; Brünink, D.; Doltsinis, N.L.; Faust, A.; Hermann, S.; Strassert, C.A. Dual Emissive Zn(II) Naphthalocyanines: Synthesis, Structural and Photophysical Characterization with Theory-Supported Insights towards Soluble Coordination Compounds with Visible and Near-Infrared Emission. *Int. J. Mol. Sci.* **2024**, *25*, 2605. <https://doi.org/10.3390/ijms25052605>

Academic Editor: Dongho Kim

Received: 31 December 2023

Revised: 9 February 2024

Accepted: 14 February 2024

Published: 23 February 2024



Copyright: © 2024 by the authors. Licensee MDPI, Basel, Switzerland. This article is an open access article distributed under the terms and conditions of the Creative Commons Attribution (CC BY) license (<https://creativecommons.org/licenses/by/4.0/>).

Abstract: Metal phthalocyanines and their higher homologues are recognized as deep-red luminophores emitting from their lowest excited singlet state. Herein, we report on the design, synthesis, and in-depth characterization of a new class of dual-emissive (visible and NIR) metal naphthalocyanines. A 4-*N,N*-dimethylaminophen-4-yl-substituted naphthalocyaninato zinc(II) complex (**Zn-NMe₂Nc**) and the derived water-soluble coordination compound (**Zn-NMe₃Nc**) exhibit a near-infrared fluorescence from the lowest ligand-centered state, along with a unique push-pull-supported luminescence in the visible region of the electromagnetic spectrum. An unprecedentedly broad structural (2D-NMR spectroscopy and mass spectrometry) as well as photophysical characterization (steady-state and time-resolved photoluminescence spectroscopy) is presented. The unique dual emission was assigned to two independent sets of singlet states related to the intrinsic Q-band of the macrocycle and to the push-pull substituents in the molecular periphery, respectively, as predicted by TD-DFT calculations. In general, the elusive chemical aspects of these macrocyclic compounds are addressed, involving both reaction conditions, thorough purification, and in-depth characterization. Besides the fundamental aspects that are investigated herein, the photoacoustic properties were exemplarily examined using phantom gels to assess their tomographic imaging capabilities. Finally, the robust luminescence in the visible range arising from the push-pull character of the peripheral moieties demonstrated a notable independence from aggregation and was exemplarily implemented for optical imaging (FLIM) through time-resolved multiphoton micro(spectro)scopy.

Keywords: dual fluorescence; multiscale-multimodal imaging; photoacoustic/optoacoustic spectroscopy; steady-state and time-resolved multiphoton micro(spectro)scopy (FLIM); (TD-)DFT

1. Introduction

Over the past decade, there has been a rising interest in the design and synthesis of compounds exhibiting dual emission (DE) [1]. While most organic molecules typically manifest a single characteristic fluorescence, certain distinctive luminophores, wherein electron donor and electron acceptor moieties are connected by a single bond, may exhibit a dual emission [2]. The phenomenon of dual fluorescence (DF) was initially observed for 4-(dimethylamino)benzonitrile (DMABN) by Lippert et al. [3]. It arises from two distinct conformations of the same molecule in the first excited singlet state (S_1), specifically, the

locally excited state (LE) and the intramolecular charge-transfer state (ICT) [4]. Subsequently, several other systems were designed incorporating a strong electron-donating or -withdrawing group [5–11]. Owing to their nonlinear optical properties, these compounds have been extensively explored as part of the development of organic materials, serving various applications including their use as electrooptical switches, chemical sensors, and fluorescent markers [12–15].

Generally, due to their broad application range as functional materials for semiconductors, gas sensors, nonlinear optical limiters, liquid crystals and as sensitizers for photodynamic therapy (PDT) in cancer treatments, among many others, metal phthalocyanines (Pcs) are counted among the most extensively investigated dyes in history, besides others such as cyanine colorants and BODIPY derivatives [16–18]. Metal naphthalocyanines (Ncs) constitute expanded analogues of their Pc counterparts that possess a linearly annulated benzene ring in the periphery of the macrocyclic core that leads to an about 100 nm red shift of the absorption band in the red if compared with Pcs. This shift, known as the rule of “100 nm”, results from the destabilization of the HOMO (highest occupied molecular orbital) and the associated decrease in the HOMO-LUMO (lowest unoccupied molecular orbital) gap [19]. Thus, Ncs are able to act as versatile tetradentate chelators for various metals and show a strong absorption in the near-infrared region (750–900 nm) with high molar absorption coefficients. The intense absorption and fluorescence bands of naphthalocyanines in the near-infrared offers interesting opportunities such as the fabrication of high-performance NIR photodiodes and bioimaging [20,21], and the complexation of open-shell or late-transition element cations can add further functionalities related to spin–spin or spin–orbit coupling, respectively.

The structural flexibility of Ncs has been extensively illustrated through a diverse range of metal complexes and a wide array of substituents that can be attached to the periphery of the core or as axial ligands [19,22–27]. This chemical modification induces specific alterations in the electronic structure of the macrocyclic core, providing precise control over the physicochemical characteristics. However, despite their ability to absorb in the far red/near-infrared region, Ncs have been relatively neglected, mainly because of their intricate synthesis, with difficult purification, poor solubility, and a tendency to form inactive aggregates, owing to strong *van der Waals* interactions upon stacking [28,29]. As a consequence of their high tendency to form aggregates, a drop of fluorescence and singlet oxygen quantum yields is observed [30,31]. There have been several structural variations introduced to overcome the solubility and aggregation issues of (na)phthalocyanines, including the insertion of bulky substituents in the peripheral positions of the macrocycles [25,32–35], the addition of axial ligands to the central atom [28,30,36–39], or the encapsulation of the dye in colloidal particles [40,41]. Furthermore, peripheral functional groups in Ncs macrocycles may be utilized to further tailor intra- and intermolecular interactions as well as optical, photochemical, and electrochemical properties; particularly, aromatic groups increase intermolecular π - π interactions [19,34]. However, all these derivatives still exhibit a strong tendency to aggregate in aqueous media, which can significantly reduce their performance due to self-quenching [42]. In the case of Pcs, these issues were solved by the introduction of several hydrophilic and amphiphilic groups (e.g., carboxylates, sulfonates, phosphonates, PEG chains) [43–48], as well as bulky axial ligands (e.g., $-\text{OSiMe}_2(\text{CH}_2)_3\text{NMe}_2$ and $-\text{OCH}(\text{CH}_2\text{NMe}_2)_2$) [49–53] in the periphery of the macrocycle or at the central atom, respectively. Among these strategies, positively charged macrocycles are of particular interest, as they might target highly vulnerable intracellular sites and produce effective DNA damage in the context of phototherapy [42]. Moreover, positively charged Pcs have been successfully employed for the photoinactivation of both Gram-negative and Gram-positive bacteria [54–56]. However, in the case of water-soluble Ncs, the majority of the reported exemplars are based on silicon(IV)-based coordination compounds, mainly due to the presence of two axial positions that can be readily modified to reduce aggregation while improving solubility in aqueous media [27,57]. While peripherally substituted water-soluble Pcs have been widely discussed in the literature [30,58], their Ncs counterparts with aque-

ous solubility have remained vastly unexplored [29,59]. Despite exhibiting NIR absorption and emission, Ncs exhibiting dual fluorescence (vis/NIR) have not been reported so far.

With this background in mind, we herein report on an unprecedented design pattern for single-component yet dual-emissive zinc(II) naphthalocyaninates, including a detailed synthesis as well as a structural and photophysical characterization. In order to suppress the intermolecular interactions and to improve their solubility, we aimed at the tailored substitution on the γ -position of the macrocyclic ligand to introduce eight 4-*N,N*-dimethylaminophen-4-yl moieties, which were further quaternized with methyl iodide to enhance their hydrophilicity. Moreover, substitution with 4-*N,N*-dimethylaminophen-4-yl moieties opens up new possibilities for push–pull-based two-photon excitability and aggregation-independent luminescence in the visible region of the electromagnetic spectrum. To assess the charge-transfer nature of the excited state that was provided by the dimethylamino substituents, an analogous 4-methoxyphen-4-yl-substituted zinc(II) naphthalocyaninate was synthesized. The assignment of the emissive states was carried out by TD-DFT calculations while rationalizing the electronic transitions dominating the absorption and emission spectra of these complexes. Thus, we anticipate that this strategy for preparing dual-emissive (visible and NIR) naphthalocyanines will pave the way for future innovation and accelerated developments in a broad range of application fields, including optoelectronics, energy conversion, and as contrast agents that are able to provide two orthogonal readouts for multiscale–multimodal imaging.

2. Results and Discussion

2.1. Design, Synthesis, Purification, and Structural Characterization

The peripheral functionalization was achieved by means of a Suzuki–Miyaura coupling reaction between 6,7-dibromo-2,3-dicyanonaphthalene (**1**) and the corresponding boronic acids, following our previously reported methodology [60]. This substitution pattern was chosen in accordance with our recent report showing that the push–pull character and perpendicular-to-plane rigidified arrangement of the two phenyl moieties can provide strong luminescence in aggregates as well as in solution. The detailed synthetic procedure is shown in Section 3 (*vide infra*). The substituted naphthalonitriles **NMe₂** and **OMe** were converted into the corresponding naphthalocyaninato zinc(II) complexes **Zn-OMeNc** and **Zn-NMe₂Nc** by refluxing them in isoamyl alcohol (*i*-amOH) in the presence of 1,8-diazabicycloundec-7-ene (DBU) in catalytic amounts (Figure 1).

The reaction was performed under inert conditions in order to prevent the oxidation of the macrocycle by atmospheric oxygen at high temperatures. The obtained products contained some fluorescent impurities (most likely low-molecular-weight condensates preceding the cyclotetramerization); attempts to use column chromatography with silica or alumina as stationary phases in combination with classical organic solvent gradients failed, as the polar components of the reaction mixture strongly bind to both materials. Reverse-phase silica was also explored for purification; also in this case, it was observed that the product strongly binds to the stationary phase. Thus, the crude reaction mixture was subjected to multiple Soxhlet extractions to remove bulk impurities. The obtained products were further purified by size exclusion chromatography (Sephadex LH-20, Amersham Pharmacia Biotech AB, Uppsala, Sweden) in *N,N*-dimethylformamide (DMF). Finally, the water-soluble octa-cationic zinc(II) naphthalocyaninate **Zn-NMe₃Nc** was obtained by treating **Zn-NMe₂Nc** with an excess of methyl iodide in DMF (Figure 2). Besides UV-vis absorption spectroscopy, the Ncs were structurally characterized by means of mass spectrometry and NMR spectroscopy. Due to their intrinsic aggregation tendency, attaining well-resolved ¹H- and ¹³C-NMR spectra proved to be particularly challenging. Nonetheless, we were able to obtain precise 2D-NMR spectra (including an unambiguous assignment for all peaks).

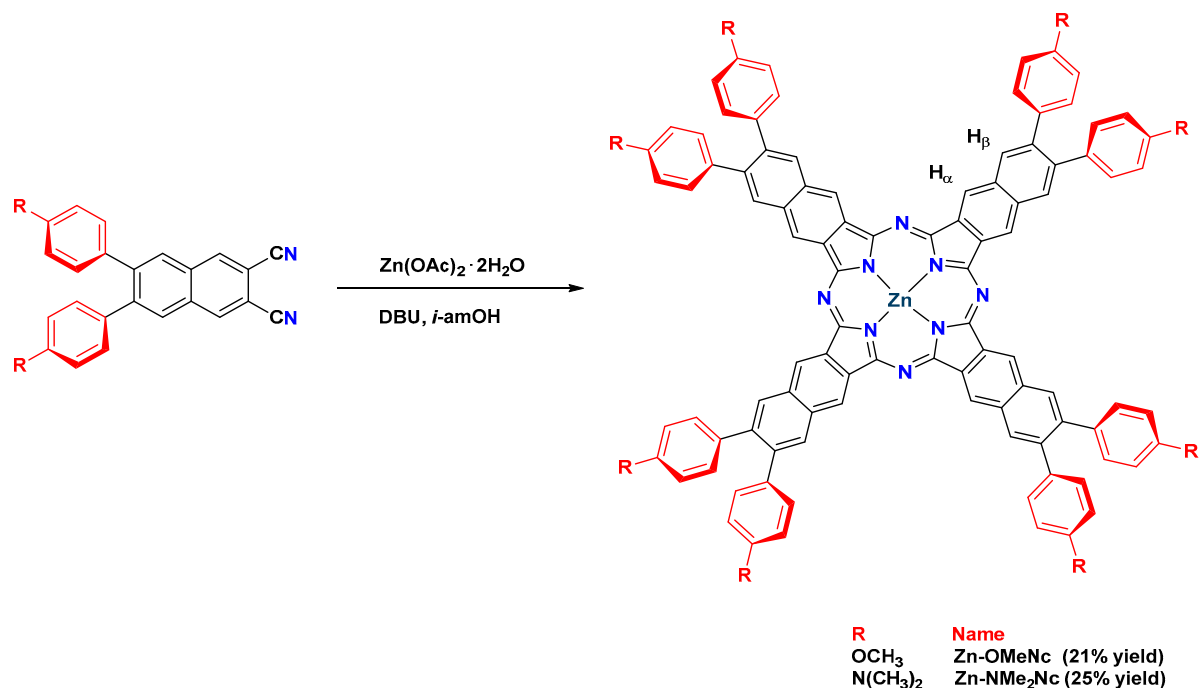


Figure 1. Synthesis of zinc(II) naphthalocyaninates.

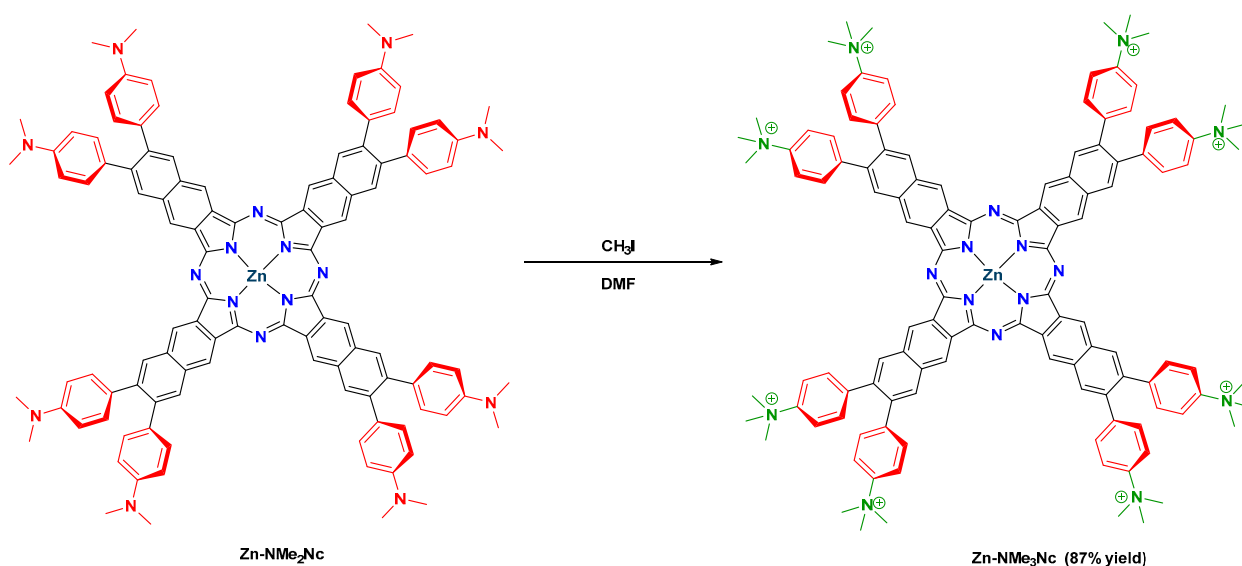


Figure 2. Synthesis of 3,4,12,13,21,22,30,31-octakis(4-(*N,N,N*-trimethylammonium)phenyl)-2,3-naphthalocyaninato zinc(II) (Zn-NMe₃Nc).

In order to obtain a better resolution in the ¹H-NMR spectra of Zn-OMeNc, Zn-NMe₂Nc, and Zn-NMe₃Nc, DMSO was used as the solvent in NMR spectroscopy, as it suppresses aggregation caused by stacking. Due to the de-shielding effect of the porphyrin core, a clear downfield shift of H_α protons compared to H_β was observed [34]. The interpretation of all signals in the ¹H-NMR spectra of the Ncs Zn-OMeNc, Zn-NMe₂Nc, and Zn-NMe₃Nc were enabled by ¹H-¹H-COSY, ¹H-¹³C-HSQC, ¹H-¹³C-HMBC, and ¹H-¹H-ROESY spectroscopies, where all signals were unambiguously assigned (also for the naphthalonitriles, see SI, Figures S1–S26). From the ¹H-NMR spectra of Zn-OMeNc and Zn-NMe₂Nc, it was clear that these two coordination compounds aggregate at the required concentrations, whereas the eight positive charges in the periphery of Zn-NMe₃Nc suppressed aggregation and yielded well-resolved ¹H-NMR spectra (Figure S21). Hence,

the proton signals from **Zn-NMe₃Nc** were better resolved than those from **Zn-OMeNc** and **Zn-NMe₂Nc**. In the ¹H-¹H-ROESY spectra, cross-peaks were observed between the signals of H_α and H_β protons and between the protons of the phenyl groups and signals corresponding to H_β (see SI, Figures S14, S20 and S26). From ¹H-¹H-COSY, additional groups of cross-peaks were found between the protons of the phenyl groups (see SI, Figures S11, S17 and S23). The mass spectra of **Zn-NMe₃Nc** were obtained by using ESI-EM, whereas for **Zn-OMeNc** and **Zn-NMe₂Nc**, MALDI-TOF had to be employed. The MS demonstrated a good agreement between the expected and observed peaks (see SI, Figures S27–S31).

2.2. UV-Vis Absorption, Steady-State, and Time-Resolved Photoluminescence Spectroscopies

In agreement with the characteristic spectroscopic features of metal (na)phthalocyanines, the UV-vis absorption spectra of the herein reported complexes feature a *Soret*-band (or B-band) in the UV range and Q-band in the NIR region [25]. Figure 3 depicts the absorption spectra of **Zn-OMeNc**, **Zn-NMe₂Nc**, and **Zn-NMe₃Nc** in DMSO and in water. A red shift of the Q-band was observed when going from **Zn-OMeNc** (794 nm) to **Zn-NMe₂Nc** (800 nm), implying that the energy gap between the HOMO and the LUMO is reduced when introducing a stronger electron π -donor (i.e., replacement of methoxy by dimethylamino moieties) [61,62]. Consistently, in the case of **Zn-NMe₃Nc**, a blue shift was observed (781 nm) in DMSO, due to the reduced electron-donating capacity of the cationic trimethylammonium groups (Table 1).

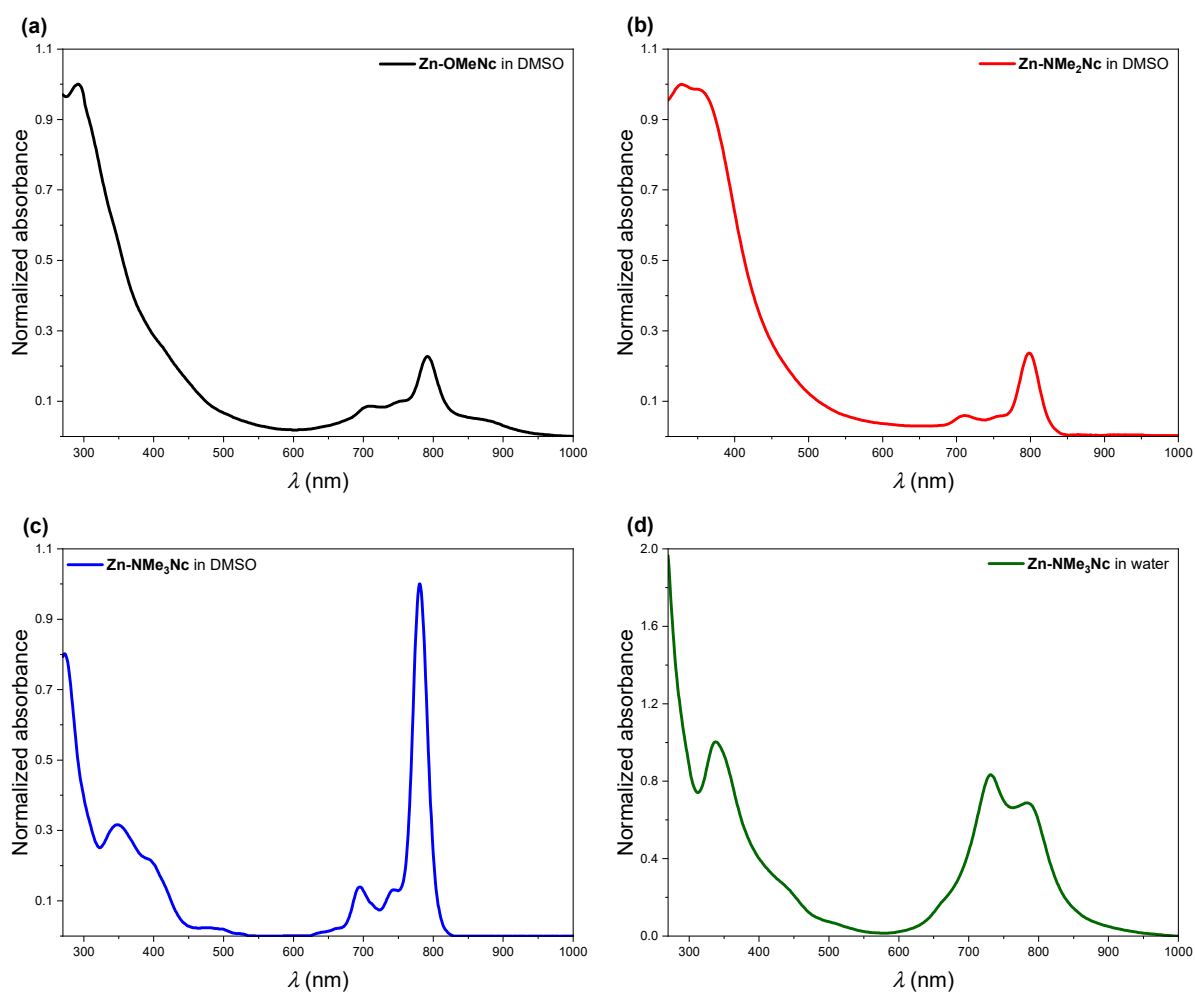


Figure 3. UV-vis absorption spectra normalized at the corresponding λ_{\max} for **Zn-OMeNc** (a), **Zn-NMe₂Nc** (b), and **Zn-NMe₃Nc** (c) in DMSO, as well as for **Zn-NMe₃Nc** in water (d).

Table 1. Q- and B-bands observed in the absorption spectra. The corresponding molar absorption coefficient (ϵ) for each band is also listed in square brackets.

Compound/ Solvent	Q-Band (λ_{\max}/nm) [$\epsilon/10^4 \text{ M}^{-1} \text{ cm}^{-1}$]	B-Band (λ_{\max}/nm) [$\epsilon/10^5 \text{ M}^{-1} \text{ cm}^{-1}$]
Zn-OMeNc/DMSO	794 [4.4]	293 [1.9]
Zn-NMe ₂ Nc/DMSO	800 [5.3]	350 [2.0]
Zn-NMe ₃ Nc/DMSO	781 [55]	350 [1.8]
Zn-NMe ₃ Nc/H ₂ O	732, 784 [22], [18]	340 [2.7]

As shown in Figure 3a,b, the Q-band appears to be less intense than the B-band, which is surprising when considering that the latter is usually weaker in metal (na)phthalocyaninates. This observation can be attributed to the strong absorption in the blue and in the UV related to the eight methoxy- or dimethylamino-substituted moieties, which actually exhibit a sizeable push–pull character (in fact, this blue-shifted band is drastically reduced upon quaternization, as seen by the comparison of Zn-NMe₂Nc with its derivative Zn-NMe₃Nc; *vide infra* regarding the additional influence of aggregation phenomena on the relative intensities in the red and in the blue region of the spectrum). Similar trends were previously reported for Zn(II) phthalocyanines [63,64]. The formation of red-shifted aggregates plays a role in the case of Zn-OMeNc, in agreement with the broadened signals that are observed in NMR spectroscopy (see SI, Figure S9); hence, the low molar absorption coefficient (ϵ) at $\lambda_{\max} = 794 \text{ nm}$ ($\epsilon = 4.4 \times 10^4 \text{ M}^{-1} \text{ cm}^{-1}$) and the rather weak absorption band at around 876 nm point towards *J*-aggregation. Similarly, in the case of Zn-NMe₂Nc, the intensity of the Q-band appears to be reduced if compared with the B-band, an observation that is reinforced by aggregation; therefore, a relatively low molar absorption coefficient at $\lambda_{\max} = 800 \text{ nm}$ ($\epsilon = 5.3 \times 10^4 \text{ M}^{-1} \text{ cm}^{-1}$) is measured. Typically, the values for Q-bands in metal (na)phthalocyaninates are of the order of $10^5 \text{ M}^{-1} \text{ cm}^{-1}$. Thus, by comparison of the three compounds presented herein, it is clear that the relatively high intensity of the B-band is prominently enhanced in the cases of Zn-OMeNc and Zn-NMe₂Nc, due to the charge-transfer absorption of the eight aromatic electron-donating moieties (methoxy- or dimethylaminophenyl, respectively), which overlap with the B-band and disappear upon quaternization (*vide infra*); in addition, aggregation compromises the intensity of the Q-band.

Nonetheless, the eight positive charges of Zn-NMe₃Nc suppress aggregation in DMSO, and the relative intensity of the Q-band vs. the B-band fall in the expected range for metal (na)phthalocyaninates [25,65]. However, the absorption spectrum of Zn-NMe₃Nc in water showed clear differences when compared to its spectrum in DMSO. In water, Zn-NMe₃Nc still exhibits *H*-aggregation, as evidenced by the presence of two non-vibrational shoulders in the Q-band region (Figure 3d). The lower energy (red-shifted) band at about 784 nm can be attributed to the monomeric species, whereas the higher energy (blue-shifted) band at 732 nm suggests the presence of *H*-aggregates, as it was previously reported for comparable (na)phthalocyanines [29–31,66]. The formation of *H*-aggregates in water is more evident when comparing the molar absorption coefficients (ϵ) of Zn-NMe₃Nc in DMSO vs. water. In DMSO, the *H*-aggregates are disrupted, and Zn-NMe₃Nc shows a characteristically high ϵ value at $\lambda_{\max} = 781 \text{ nm}$ ($\epsilon = 5.5 \times 10^5 \text{ M}^{-1} \text{ cm}^{-1}$). This contrasts with the spectrum in water, where Zn-NMe₃Nc peaks at $\lambda_{\max} = 732 \text{ nm}$ ($\epsilon = 2.2 \times 10^5 \text{ M}^{-1} \text{ cm}^{-1}$), and $\lambda_{\max} = 784 \text{ nm}$ ($\epsilon = 1.8 \times 10^5 \text{ M}^{-1} \text{ cm}^{-1}$) (Table 1). In water, *H*-aggregation reduces the Q-band intensity with respect to the B-band, and the molar absorption coefficient in the red drops by a factor of roughly two, which points toward dimerization. Despite the clear aggregation phenomena discussed above, the Lambert–Beer law was obeyed within the experimental range for all these compounds (see SI, Figures S35–S47) [67]. In general, the molar absorption coefficients were obtained from the slope of the absorbance versus

the concentration of the samples (the latter were determined by total reflection X-ray fluorescence (TXRF) addressing the concentration of Zn).

The UV-vis absorption, steady-state photoluminescence emission and excitation spectra of **Zn-OMeNc**, **Zn-NMe₂Nc**, and **Zn-NMe₃Nc** were measured in DMSO (Figure 4). In the case of **Zn-NMe₃Nc** in water, a clear narrowing of the excitation spectrum was observed compared with the absorption spectrum, as only the emissive monomers were addressed, whereas all species (even aggregates) in a solution contribute to the broadened absorption. The proximity of the Q-band-related emission with respect to the Q-band excitation and absorption for **Zn-OMeNc**, **Zn-NMe₂Nc**, and **Zn-NMe₃Nc** in DMSO indicate that the nuclear configurations of the ground and excited states are comparable and therefore practically not affected by the excitation wavelength.

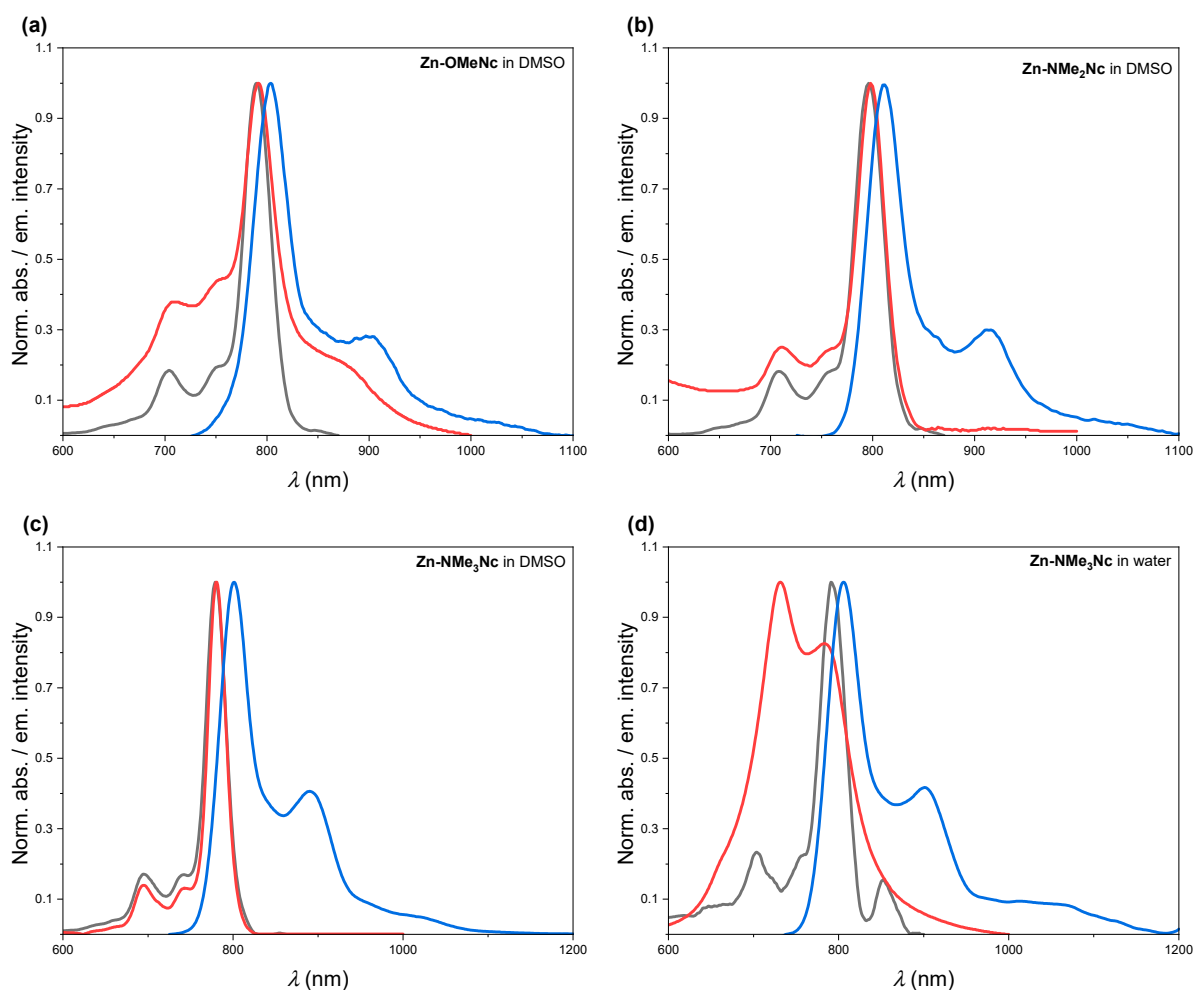


Figure 4. Absorption (red), excitation (black, $\lambda_{em} = 920$ nm), and emission (blue, $\lambda_{ex} = 750$ nm) spectra of **Zn-OMeNc** (a), **Zn-NMe₂Nc** (b), **Zn-NMe₃Nc** in DMSO (c) and **Zn-NMe₃Nc** in water (d).

In agreement with previous reports on metal (na)phthalocyaninates, the photoluminescence emission spectra of **Zn-OMeNc**, **Zn-NMe₂Nc**, and **Zn-NMe₃Nc** mirror the excitation spectra with a typically small Stokes shift (Figure 4), if referring to the red-shifted Q-band. As can be observed in the full-range emission spectra (recorded while exciting in the UV), the compounds feature a surprisingly prominent dual emission, which will be discussed below (*vide infra*). This phenomenon was initially noticed while measuring the emission spectra of **Zn-NMe₂Nc** in DMSO at different excitation wavelengths (λ_{ex}). After varying λ_{ex} , a broad emission band with a $\lambda_{em} = 560$ nm ($\lambda_{ex} = 335$ nm) and a sharp near-infrared emission with $\lambda_{em} = 811$ nm ($\lambda_{ex} = 750$ nm) was observed (Figure 5c,d, Table 2). In order to understand this rather unique dual emission, the analogous **Zn-OMeNc** was also designed,

prepared, and studied. Interestingly, **Zn-OMeNc** also exhibited two clear emission bands, with a $\lambda_{em} = 508$ nm ($\lambda_{ex} = 335$ nm) and $\lambda_{em} = 804$ nm ($\lambda_{ex} = 750$ nm) in DMSO (Figure 5c,d, Table 2). It is important to mention that when using $\lambda_{ex} = 335$ nm and screening the emission from the blue to the NIR region to acquire the full-range fluorescence spectra, both bands are visible in the case of **Zn-OMeNc** and **Zn-NMe₂Nc** (Figure 5a,b, Table 2).

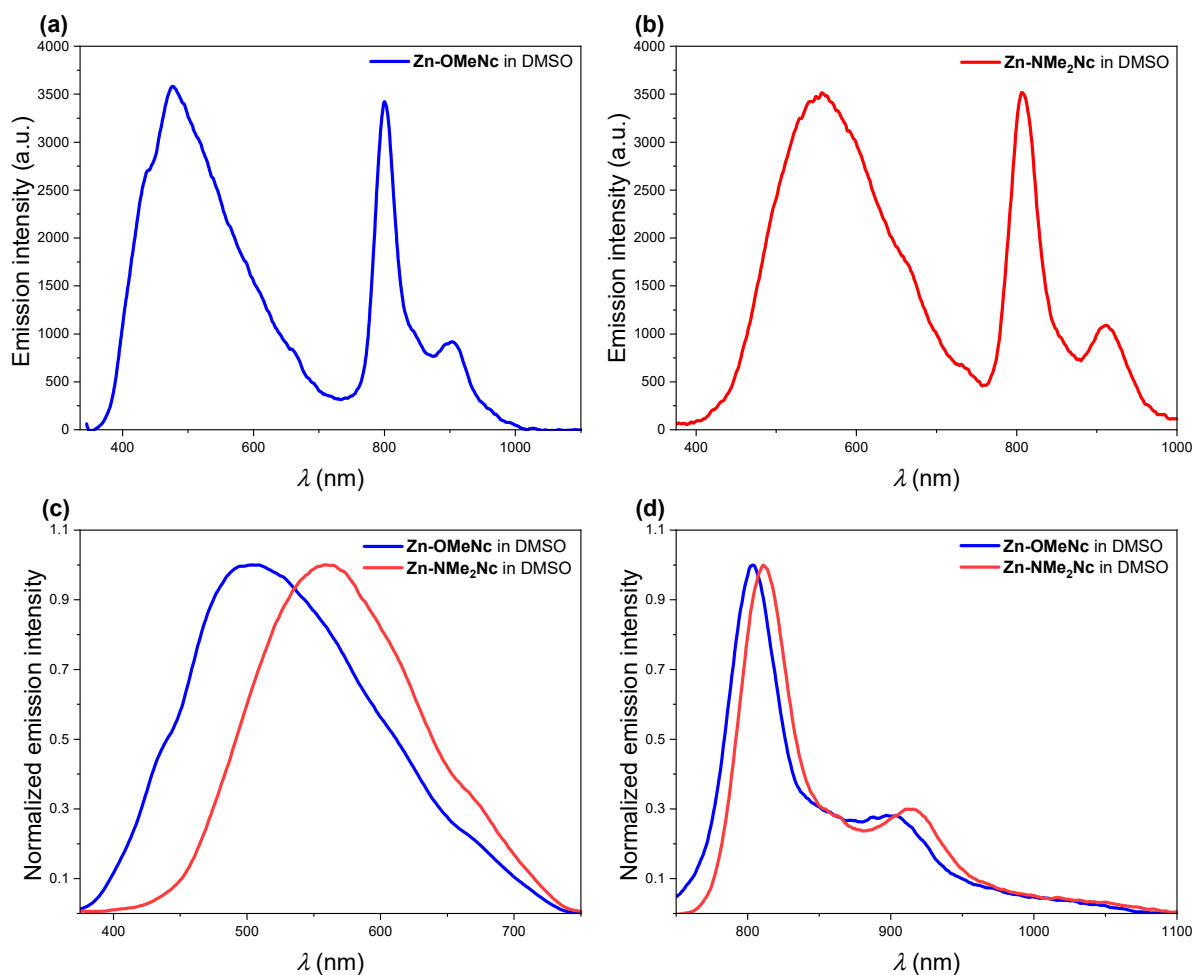


Figure 5. Fluorescence in DMSO: (a) full-range emission spectrum of **Zn-OMeNc** (blue), $\lambda_{ex} = 335$ nm; (b) full-range spectrum of **Zn-NMe₂Nc** (red), $\lambda_{ex} = 335$ nm; (c) normalized emission spectra of **Zn-OMeNc** (blue) and **Zn-NMe₂Nc** (red) in the visible region, $\lambda_{ex} = 335$ nm; (d) normalized emission spectra of **Zn-OMeNc** (blue) and **Zn-NMe₂Nc** (red) in the near-infrared region, $\lambda_{ex} = 750$ nm. In the full-range emission spectra (a,b), the bands may appear slightly different (if compared with (c,d), both in shape and intensity), due to the different instrumental settings and filters employed (for details, see Section 3.3).

A similar trend was observed for **Zn-NMe₃Nc** when measured in water and in DMSO. In DMSO, **Zn-NMe₃Nc** exhibited two emission bands, with a $\lambda_{em} = 550$ nm ($\lambda_{ex} = 335$ nm) and $\lambda_{em} = 801$ nm ($\lambda_{ex} = 750$ nm) (Figure 6c,d, Table 2). In contrast, the emission bands measured in water were observed at $\lambda_{em} = 432$ nm ($\lambda_{ex} = 335$ nm) and $\lambda_{em} = 804$ nm ($\lambda_{ex} = 750$ nm) (Figure 6c,d, Table 2). When a full-range emission spectrum for **Zn-NMe₃Nc** in DMSO was measured (from blue to the NIR region using $\lambda_{ex} = 335$ nm), a relatively faint emission band with $\lambda_{em} = 550$ nm and a high-intensity luminescence with $\lambda_{em} = 800$ nm were observed (Figure 6a). This can be attributed to the reduction in the push-pull character upon quaternization of the peripheral 4-*N,N*-dimethylaminophen-4-yl groups and the monomeric nature of **Zn-NMe₃Nc** in DMSO, yielding a comparably strong NIR fluorescence and a weak visible emission. Thus, it is inferred that the monomers of **Zn-NMe₃Nc**

in DMSO yield an intense NIR emission and a comparatively weak luminescence between 400 nm and 500 nm. In contrast, the full-range emission spectrum of **Zn-NMe₃Nc** in water (from blue to the NIR region using $\lambda_{\text{ex}} = 335$ nm) exhibited a substantially stronger emission band, peaking at $\lambda_{\text{em}} = 400$ nm, when compared with the NIR fluorescence band at $\lambda_{\text{em}} = 801$ nm (Figure 6b); this can be understood when taking into account that in water, *H*-aggregation suppresses the fluorescence in the NIR, and a comparatively strong residual emission remains in the visible range. The dual emission of **Zn-OMeNc**, **Zn-NMe₂Nc**, and **Zn-NMe₃Nc** was interpreted and assigned by TD-DFT calculations (*vide infra*).

Table 2. Photophysical properties of the compounds (λ_{max} and τ). P1 and P2 are the peaks in the visible and NIR regions in the emission spectra, respectively. For the bi-exponential photoluminescence decays, the amplitude-weighted average lifetimes ($\tau_{\text{av_amp}}$) are shown. The τ values are rounded to match the significant figures of the uncertainties; raw time-resolved photoluminescence decays and fitting parameters are shown in the SI, Figures S48–S55.

Compound/ Solvent	$\lambda_{\text{max}}/\text{nm}$ P1/P2	τ/ns [P1]	τ/ns [P2]
Zn-OMeNc /DMSO	508/804	$\tau_1 = 8.2 \pm 0.3$ (21%)	$\tau_1 = 2.05 \pm 0.03$ (68%)
		$\tau_2 = 2.7 \pm 0.1$ (79%)	$\tau_2 = 1.0 \pm 0.1$ (32%)
		$\tau_{\text{av_amp}} = 3.8 \pm 0.1$	$\tau_{\text{av_amp}} = 1.7 \pm 0.1$
Zn-NMe₂Nc /DMSO	560/811	$\tau_1 = 8.4 \pm 0.2$ (34%)	$\tau_1 = 1.80 \pm 0.08$ (21%)
		$\tau_2 = 2.3 \pm 0.2$ (61%)	$\tau_2 = 0.61 \pm 0.03$ (79%)
		$\tau_{\text{av_amp}} = 4.6 \pm 0.1$	$\tau_{\text{av_amp}} = 0.86 \pm 0.04$
Zn-NMe₃Nc /DMSO	550/801	$\tau_1 = 9.1 \pm 0.2$ (55%)	$\tau = 5.69 \pm 0.02$
		$\tau_2 = 3.4 \pm 0.4$ (45%)	
		$\tau_{\text{av_amp}} = 6.6 \pm 0.2$	
Zn-NMe₃Nc /H ₂ O	432/804	$\tau_1 = 8.5 \pm 0.4$ (9%)	$\tau_1 = 5.43 \pm 0.05$ (28%)
		$\tau_2 = 5.2 \pm 0.1$ (91%)	$\tau_2 = 1.20 \pm 0.08$ (72%)
		$\tau_{\text{av_amp}} = 5.51 \pm 0.03$	$\tau_{\text{av_amp}} = 2.4 \pm 0.1$

The dual fluorescence can be explained by two sets of singlet states (with orthogonal charge-transfer vs. main-ligand-centered character). The near infrared fluorescence originates from the $S_{1/2} \rightarrow S_0$ transition, and the visible emission stems from the $S_3 \rightarrow S_0$ transition. The doubly degenerate $S_{1/2}$ state has a $\pi-\pi^*$ character, whereas the S_3 states have a charge-transfer ($n-\pi^*$) character involving the electron-rich methoxy- or dimethylamino-substituted phenyl moieties. The energy gap between $S_{1/2}$ and S_3 states is relatively large; the lack of excited state geometry distortion (i.e., parallel potential hypersurfaces or “nested states”) hamper the non-adiabatic crossover, leading to relatively slow internal conversion processes. Hence, in the case of **Zn-OMeNc**, **Zn-NMe₂Nc**, and **Zn-NMe₃Nc**, both an emission in the visible region and an NIR fluorescence are observed. In the case of **Zn-NMe₃Nc** in water, the $S_{1/2}$ state is quenched due to aggregation, the intensity of the NIR emission is low, and the push-pull character is reduced due to quaternization.

Taking into account that the relative intensities of the two emission bands remain invariant when comparing independently synthesized batches, and considering the thorough purification that was carried out with no traces of impurities in the NMR spectra, we can confidently exclude spurious emission from side products or other contamination (photodecomposition is ruled out, as the absorption and emission spectra do not significantly vary during the photophysical characterization). Moreover, TD-DFT calculations support the assignment (*vide infra*).

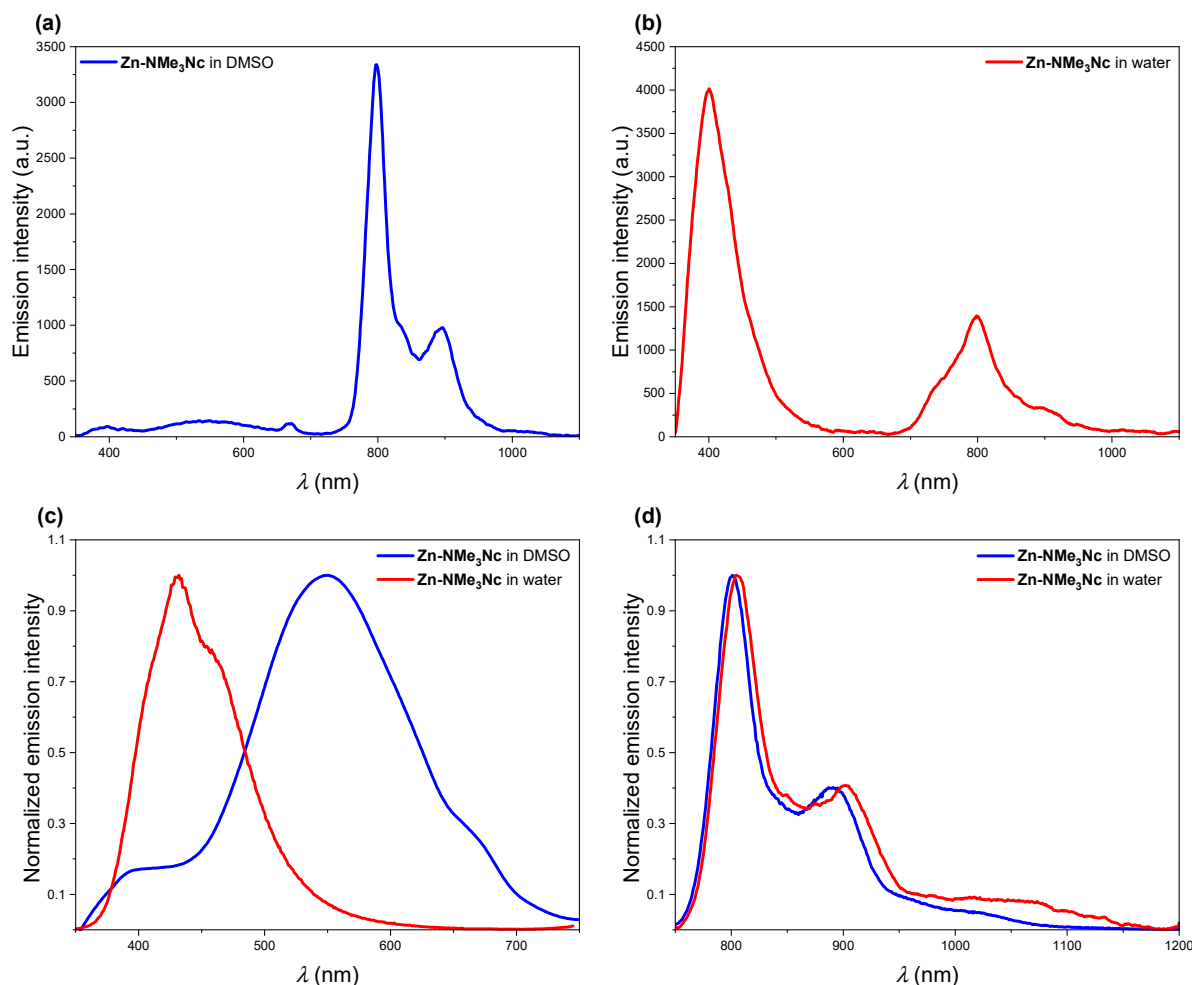


Figure 6. Fluorescence in DMSO and in water: (a) full-range emission spectrum of **Zn-NMe₃Nc** (blue) in DMSO, $\lambda_{\text{ex}} = 335$ nm; (b) full-range emission spectrum of **Zn-NMe₃Nc** (red) in water, $\lambda_{\text{ex}} = 335$ nm; (c) normalized emission spectra of **Zn-NMe₃Nc** in DMSO (blue) and water (red) in the visible region, $\lambda_{\text{ex}} = 335$ nm; (d) normalized emission spectra of **Zn-NMe₃Nc** in DMSO (blue) and water (red) in the near-infrared region, $\lambda_{\text{ex}} = 750$ nm. In the full-range emission spectra (a,b), the bands may appear slightly different (if compared with (c,d), both in shape and intensity) due to the different instrumental settings and filters employed (for details see Section 3.3).

2.3. TD-DFT Calculations

In order to assign the transitions that were observed in the absorption and fluorescence spectra, we optimized the structures of **Zn-OMeNc**, **Zn-NMe₂Nc**, and **Zn-NMe₃Nc** in their electronic ground states (for computational details, see Section 3.4). All three complexes exhibited a highly planar core, which was marginally influenced by the peripheral substituents (see Figure 7). At the optimized ground state geometries, the UV-vis absorption spectra were calculated using TD-DFT/B3LYP.

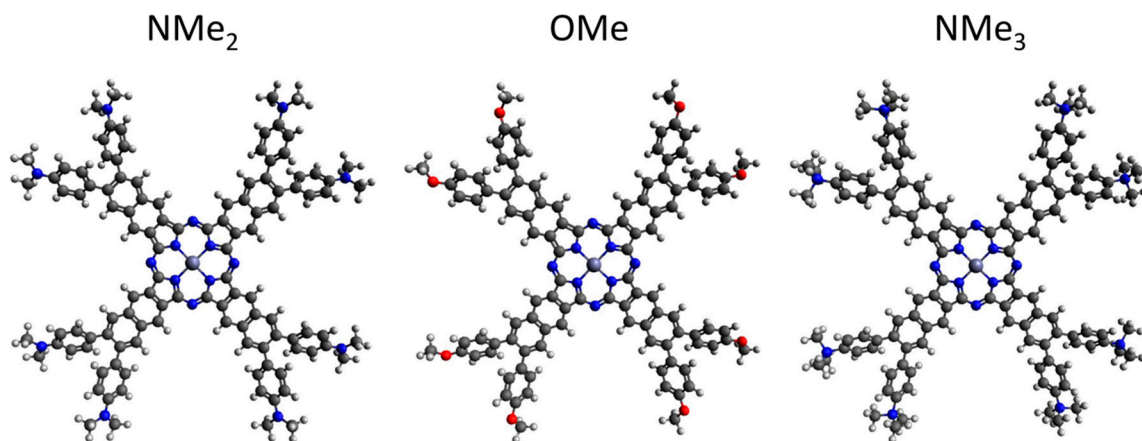


Figure 7. Optimized ground state structures of Zn-OMeNc, Zn-NMe₂Nc, and Zn-NMe₃Nc, obtained with DFT.

As can be seen from Figure 8, the theoretical spectra generally agree well with the experimental data. Due to the degeneracy of the LUMO and LUMO + 1 orbitals, the S₁ and S₂ states are also doubly degenerate, as they can be described by HOMO → LUMO and HOMO → LUMO+1 excitations, respectively. The band corresponding to the S₀ → S_{1/2} transition—located at 805 nm, 756 nm, and 740 nm for Zn-NMe₂Nc, Zn-OMeNc, and Zn-NMe₃Nc, respectively—shows a progressive blue shift with decreasing electron donor ability, in good agreement with the experimental data (and also qualitatively with respect to the relative intensities of the B- and Q-bands). The high intensity of this NIR maximum can be explained by the fact that it represents a local excitation within the 2,3-naphthalocyaninato ligand (the black part of the structure depicted in Figure 1, see Figure 9 for a visualization of the relevant frontier orbitals).

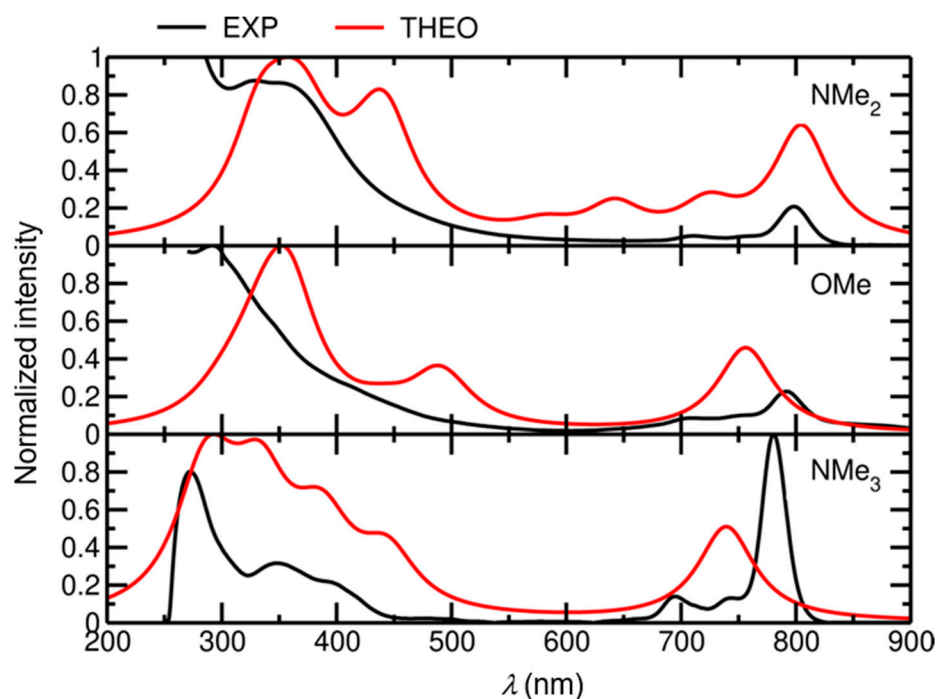


Figure 8. Calculated UV-vis absorption spectra of Zn-OMeNc, Zn-NMe₂Nc, and Zn-NMe₃Nc in DMSO (red lines), together with the corresponding experimental data (black lines).

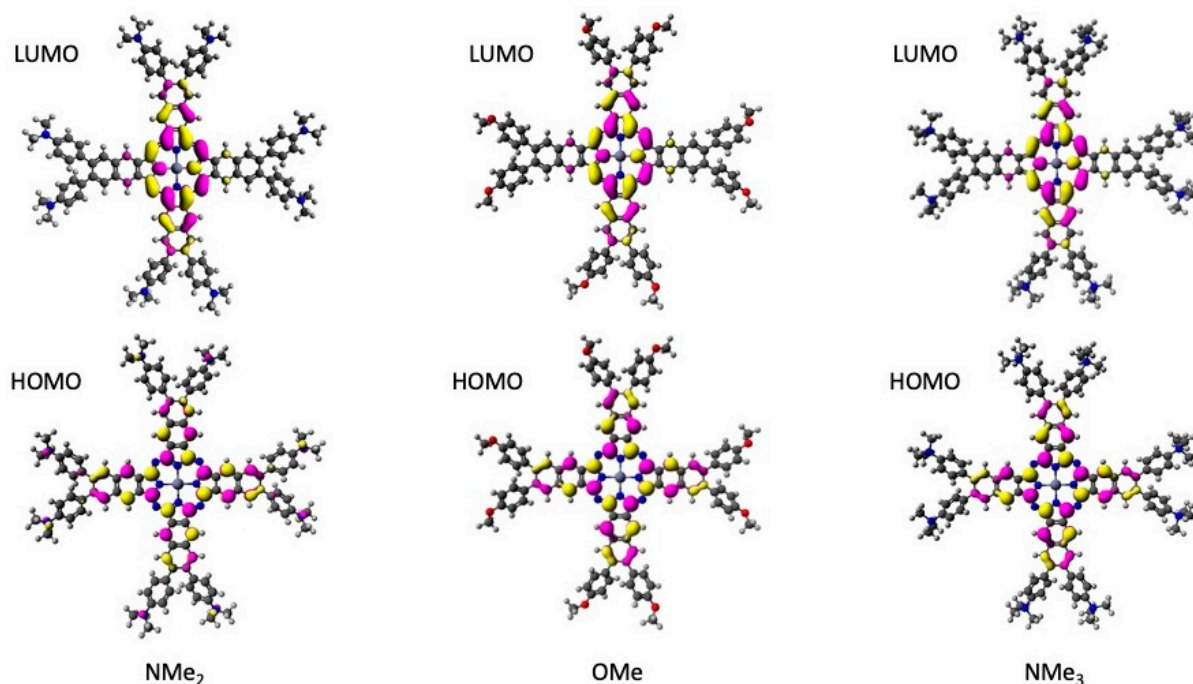


Figure 9. Isosurface plots (isovalue = 0.02) of the molecular orbitals of **Zn-OMeNc**, **Zn-NMe₂Nc**, and **Zn-NMe₃Nc**, with the highest contributions describing the $S_{1/2} \rightarrow S_0$ de-excitation.

In addition, we calculated the 0-0 fluorescence wavelengths from the $S_{1/2}$ and S_3 states by optimizing the respective excited state geometries and subtracting the optimized ground state energy. While the $S_{1/2} \rightarrow S_0$ de-excitation involved a local LUMO/LUMO + 1 \rightarrow HOMO configuration change (Figure 9), which was reasonably well described by all functionals that were tested herein, the $S_3 \rightarrow S_0$ de-excitation turned out to be much more problematic, as it involved a pronounced charge-transfer character for the relevant excited state—at least for **Zn-OMeNc** and **Zn-NMe₂Nc** (see Figure 10). For **Zn-NMe₂Nc**, geometry optimization with the B3LYP functional leads to a collapse of the S_3 state onto the $S_{1/2}$ state, yielding spurious emission wavelengths. The long-range corrected functional CAM-B3LYP, on the other hand, significantly overestimated the S_3 energy (see SI, Table S1). In fact, the PBE0 functional emerged as the best compromise for all three compounds, considering both emission lines in the visible and the NIR (see Figure 11). It is able to reproduce the position of the experimental 0-0 peaks accurately, including the slight blue shift when going from **Zn-NMe₂Nc** to **Zn-NMe₃Nc** via **Zn-OMeNc**. For **Zn-OMeNc**, the S_3 peak was also described very well, while for **Zn-NMe₂Nc**, the agreement with the experiment was particularly poor, with the PBE0 peak being red-shifted by about 150 nm.

Presumably, this is due to the stronger charge-transfer character in the case of **Zn-NMe₂Nc**, with a notable amount of charge density being located at the NMe₂ substituent in the HOMO-1. In addition, the S_3 state contains a 7% contribution of the local HOMO \rightarrow LUMO + 1 excitation. The use of the M06-2X functional leads to a considerable improvement for **Zn-NMe₂Nc** (see Figure 11), but not for the other two compounds. PBE0 predicts the S_3 state to be governed by a HOMO-1 \rightarrow LUMO excitation in the case of **Zn-NMe₂Nc** and **Zn-OMeNc**, whereas for **Zn-NMe₃Nc**, the S_3 state is dominated by a HOMO \rightarrow LUMO + 2 excitation (Figure 10).

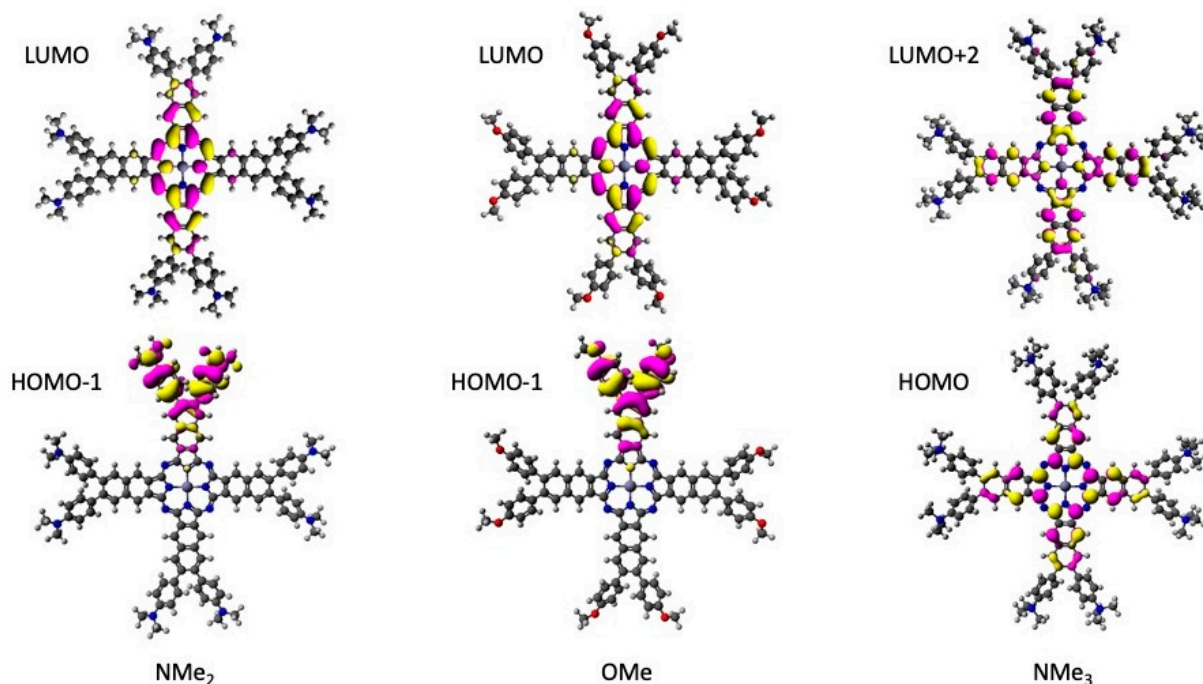


Figure 10. Isosurface plots (isovalue = 0.02) of the molecular orbitals of Zn-OMeNc, Zn-NMe₂Nc, and Zn-NMe₃Nc, with the highest contributions describing the S₃ → S₀ de-excitation.

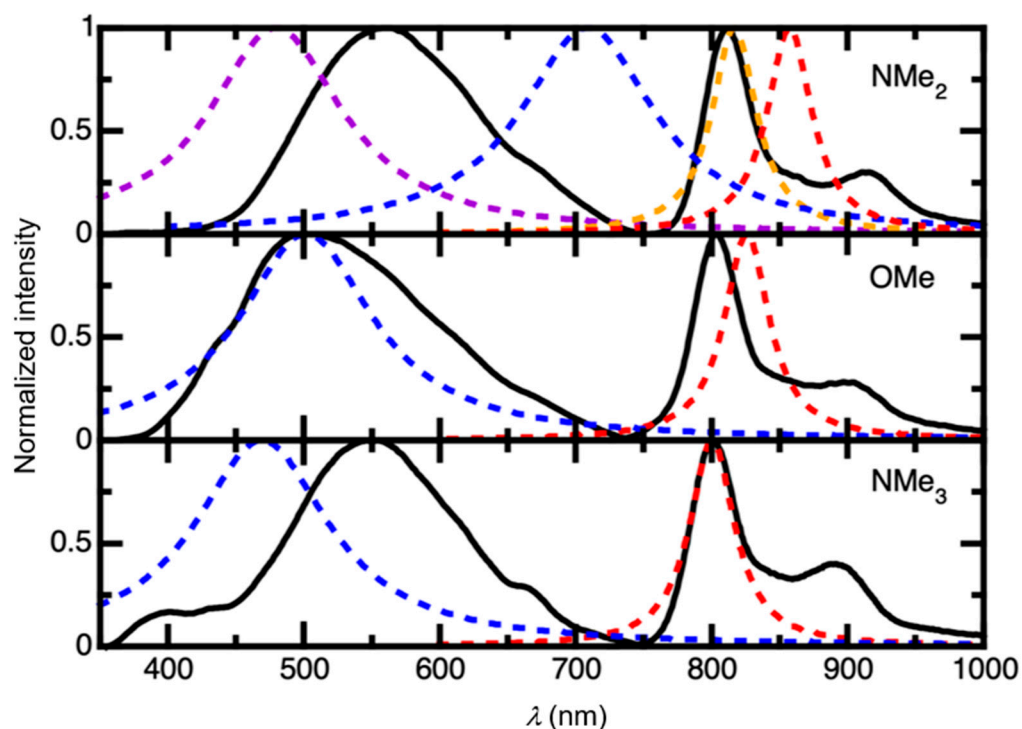


Figure 11. Calculated 0-0 emission wavelengths (dashed lines) from the S_{1/2} (red) and S₃ (blue) states, obtained with the PBE0 functional, compared to experimental fluorescence spectra (black lines) of Zn-OMeNc, Zn-NMe₂Nc, and Zn-NMe₃Nc in DMSO. For Zn-NMe₂Nc, additional results using the M06-2X functional are shown (S_{1/2} in orange, S₃ in purple).

2.4. MSOT Imaging in Gel Phantoms

In recent studies, it has been demonstrated that naphthalocyaninato complexes (Ncs) hold significant potential as photoacoustic contrast agents [27,68,69]. In comparison with

other organic compounds, such as cyanine dyes and nanoparticles, naphthalocyanines exhibit higher molar absorption coefficients in the NIR region, featuring sharp maxima between 770 nm and 850 nm [16]. The well-defined NIR absorption peaks mentioned above contribute to more precise spectral unmixing, distinguishing them from other exogenous contrast agents [70]. As a result, **Zn-NMe₂Nc** and **Zn-NMe₃Nc** were employed as representative examples for generating photoacoustic (PA) images utilizing multi-spectral photoacoustic tomography (MSOT). These measurements were conducted within tissue-mimicking gel phantoms, as depicted in Figure 12 [69]. The experiments were carried out at different concentrations, and the obtained photoacoustic profiles qualitatively agree with the absorption spectra regarding the wavelengths that induce the highest photoacoustic response. The phantom studies were performed by dissolving **Zn-NMe₂Nc** in DMSO, **Zn-NMe₃Nc** in DMSO, and **Zn-NMe₃Nc** in water, respectively.

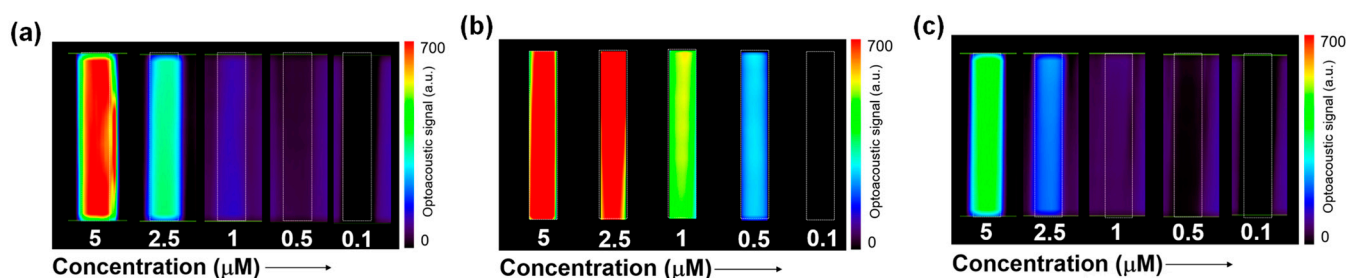


Figure 12. MSOT photoacoustic images of gel phantoms at different concentrations: (a) **Zn-Nme₂Nc** in DMSO, (b) **Zn-Nme₃Nc** in DMSO, and (c) **Zn-NMe₃Nc** in water ($\lambda_{\text{ex}} = 745$ nm).

Among these, **Zn-NMe₃Nc** in DMSO provided the highest photoacoustic signal even at a low concentration (1 μM), with **Zn-NMe₂Nc** in DMSO and **Zn-NMe₃Nc** in water showing similar yet slightly lower PA signals (Figure 13). The observed difference in signal intensity of **Zn-NMe₃Nc** in DMSO and water can be attributed to the monomerization in DMSO and aggregation in water. Also, when comparing the photoacoustic (Figure 13) and absorption spectra (Figure 3c) of **Zn-NMe₃Nc** in DMSO at $\lambda_{\text{max}} = 781$ nm, the relative intensities of the vibronic features appear distorted. For the photoacoustic spectra of **Zn-NMe₃Nc** in DMSO, the inner filter effect limits the excitation at the main maxima, even at very low concentrations (1 μM), while causing a saturation plateau between $\lambda_{\text{max}} = 781$ nm and $\lambda_{\text{max}} = 700$ nm. As **Zn-NMe₃Nc** in DMSO provides the best photoacoustic signals at a low concentration, it is clear that the suppression of aggregation enhances the photoacoustic output. In the future, this could be further improved with vanadyl- or silicon-naphthalocyanines, where the axial ligands could prevent aggregation [30,69,71]; the insertion of vanadyl centers could further shift the absorption maxima to longer wavelengths in the infrared region [72–74].

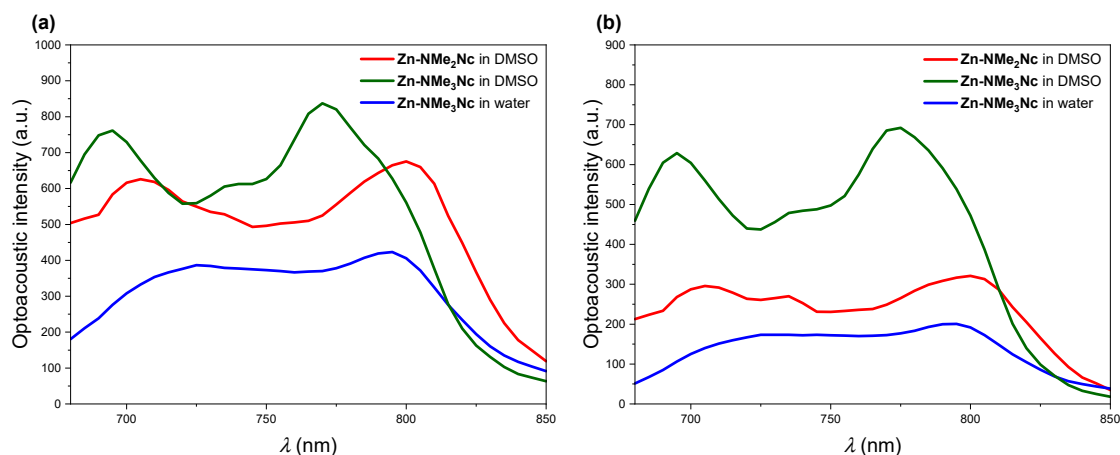


Figure 13. Cont.

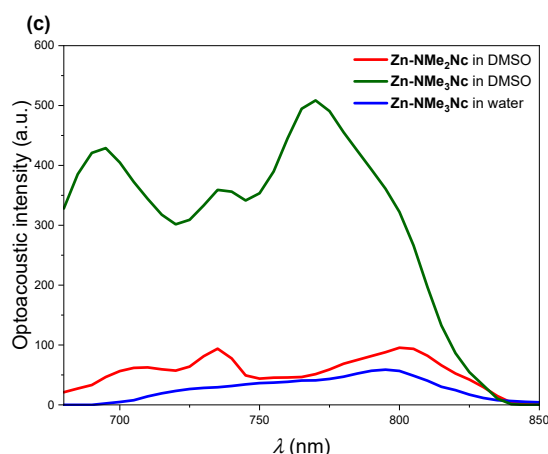


Figure 13. Photoacoustic spectra of **Zn-NMe₂Nc** in DMSO (red) and **Zn-NMe₃Nc** in DMSO (green) and water (blue) at different concentrations, obtained from reconstructed MSOT photoacoustic images. Spectra at concentration of 5 μM (a), 2.5 μM (b), and 1 μM (c).

2.5. Time-Resolved Multiphoton Micro(spectro)scopy

In order to demonstrate the ability to image structural features by time-resolved multiphoton micro(spectro)scopy, we employed **Zn-NMe₂Nc** to stain 1 μm sized aminated polystyrene microparticles (PSMPs) by a swelling–diffusion processes [75], as these are well-established models for microstructured samples (Figure 14b). As depicted in Figure 14, the photoluminescence emission spectra of **Zn-NMe₂Nc**-loaded PSMPs (**Zn-NMe₂Nc@PSMP**) in water show a broad emission band in the green ($\lambda_{\text{max}} \approx 470 \text{ nm}$), but no emission was observed in the near-infrared region (Figure 14a); this points towards aggregation-caused quenching of the fluorescence from the macrocycle, as it was previously reported for other (na)phthalocyanines [76]. However, the distinct emission in the visible region, originating from the push–pull character of the excited side groups, can be utilized as an additional optical readout, despite the lack of intrinsic luminescence from the macrocycle. In fact, the push–pull side groups have been previously introduced in our recent work as robust luminophores, both in aggregated and in monomeric forms [60]. The excited state lifetime of the stained microparticles in liquid water was determined, and a $\tau_{\text{av_amp}} = 5.1 \text{ ns}$ was obtained (Figure S56).

Further experiments were carried out to assess the photophysical properties of discrete **Zn-NMe₂Nc@PSMP**. Briefly, **Zn-NMe₂Nc@PSMP** were placed on a microscope slide and analyzed using single-photon excitation (SPE) to carry out fluorescence lifetime imaging microscopy (FLIM). As depicted in Figure 15, the particles were homogeneously stained with the push–pull luminophore, confirming the observation that is shown in Figure 14, while possessing a homogeneously distributed amplitude-weighted average lifetime of $\tau \approx 3.9 \text{ ns}$ (Figures 15 and S57). In addition, employing a spectrophotometer coupled by an optical fiber to the confocal microscope, the emission spectra of discrete **Zn-NMe₂Nc@PSMP** entities were obtained as dry samples while consistently reproducing the results for **Zn-NMe₂Nc@PSMP** that was suspended in liquid water (Figure 15). In contrast to single-photon excitation (SPE), two-photon excitation (TPE) laser scanning microscopy is often anticipated to increase cell survival and tissue penetration [77]. Thus, we explored herein a way to increase the detection sensitivity due to an improved sample penetration employing a near-infrared TPE laser; we therefore performed comparable FLIM experiments using a high-intensity Ti:Sa oscillator as the two-photon excitation source (Figure 15), where comparable photoluminescence lifetime maps were obtained. In addition, the emission spectra of discrete **Zn-NMe₂Nc@PSMP** were also measured by TPE. These experiments demonstrate that no significant differences are to be expected when using SPE and TPE (both in lifetimes (Figures S57 and S58) and in the emission spectra) for optical imaging, while providing a second readout for microscopic imaging.

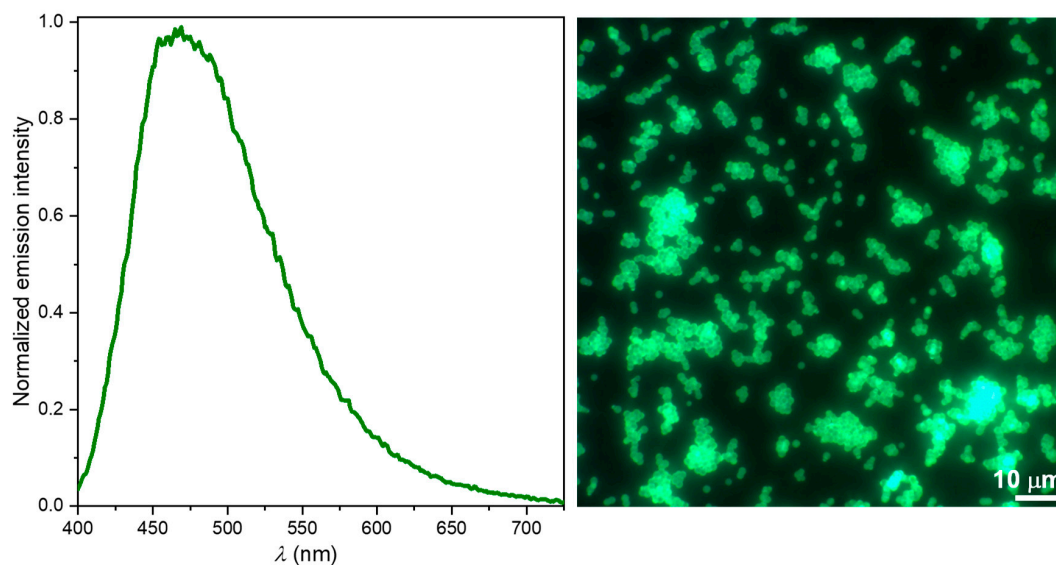


Figure 14. Left: emission spectrum of the Zn-NMe₂Nc@PSMP, suspended in H₂O ($\lambda_{\text{ex}} = 335$ nm). Right: luminescence image of the Zn-NMe₂Nc@PSMP, observed under an optical microscope (scale bar = 10 μm ; $\lambda_{\text{ex}} = 355 \pm 20$ nm).

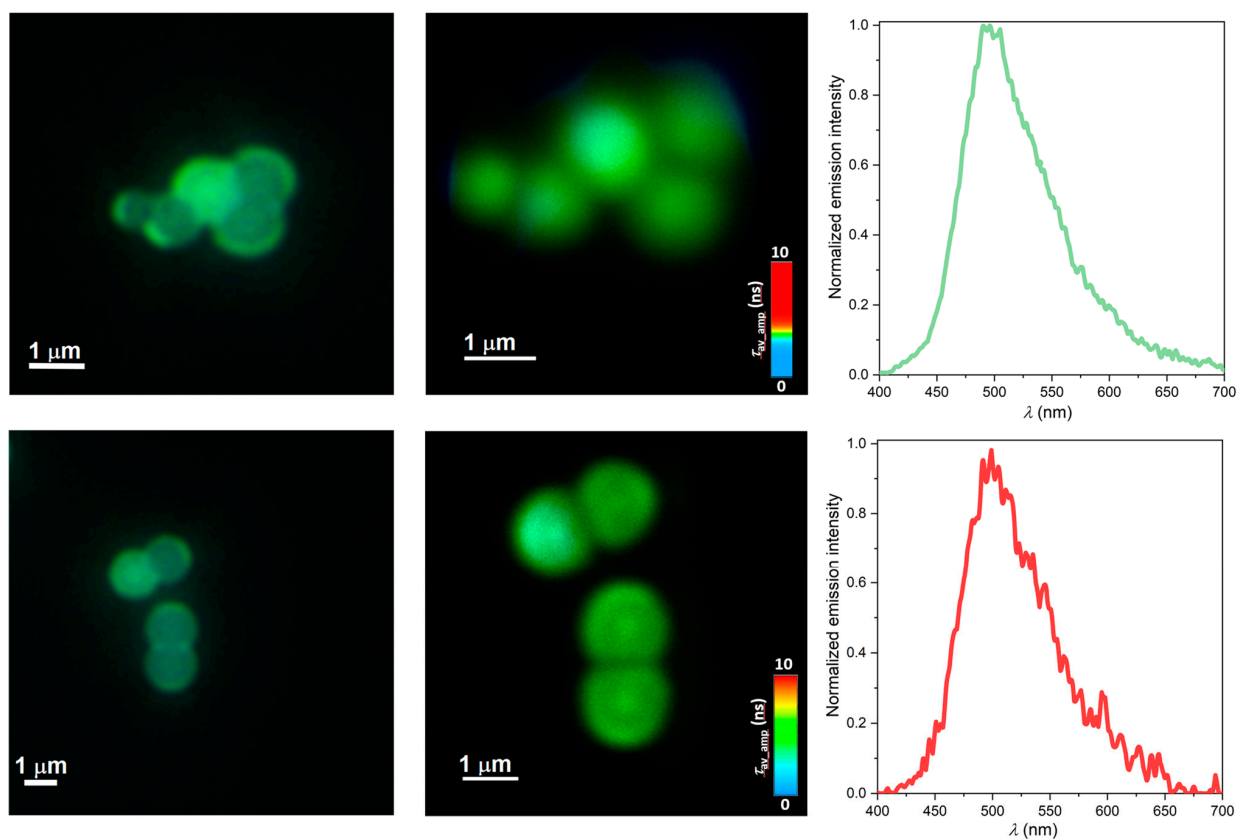


Figure 15. Upper row: Fluorescence micrograph of Zn-NMe₂Nc@PSMP (left); fluorescence lifetime map measured with single-photon excitation (SPE, $\lambda_{\text{ex}} = 375$ nm, center); emission spectrum of a discrete particle using SPE ($\lambda_{\text{ex}} = 375$ nm, right). Lower row: Fluorescence micrograph of Zn-NMe₂Nc@PSMP (left); fluorescence lifetime map measured with two-photon excitation (TPE, $\lambda_{\text{ex}} = 810$ nm, center); emission spectrum of a discrete particle using TPE ($\lambda_{\text{ex}} = 810$ nm, right). Raw photoluminescence decays and further details can be found in Figures S57 and S58.

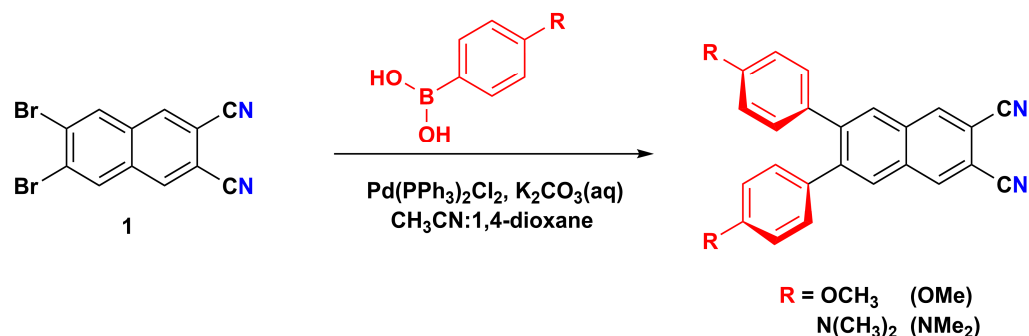
3. Materials and Methods

All chemicals were purchased with the maximum quality available from Sigma Aldrich (Taufkirchen, Germany) or from TCI Chemicals (Eschborn, Germany) and used without further purification. Reactions were carried out using dried solvents (99.9% purity) under argon atmosphere. They were monitored by thin-layer chromatography (TLC), which was performed on 0.2 mm Macherey-Nagel ALUGRAM (Eupen, Belgium) precoated silica gel aluminum sheets. Spots were visualized by a UV handlamp (254 and 365 nm). Silica gel 60 (0.063–0.200 mm, Merck, Darmstadt, Germany) was used for column chromatography, if not otherwise stated. Fresh spectroscopic-grade solvents (Uvasol[®], Merck, Darmstadt, Germany) were utilized for the spectroscopic studies.

3.1. Synthesis and Characterization of 6,7-Disubstituted Naphthalene-2,3-dicarbonitriles and Zinc(II) Naphthalocyanines

3.1.1. General Procedure for the Synthesis of 6,7-Disubstituted Naphthalene-2,3-dicarbonitriles

6,7-dibromonaphthalene-2,3-dicarbonitrile (**1**) was synthesized according to a published procedure [23,78,79]. The 6,7-disubstituted naphthalene-2,3-dicarbonitriles were obtained by Suzuki–Miyaura reactions from **1** with the corresponding boronic acids (Scheme 1) [60]. Briefly, a mixture of **1** (1 equiv.), the corresponding *p*-substituted-phenylboronic acid (4 equiv.), and a saturated aqueous solution of K₂CO₃ (5 mL) were stirred in 50 mL of a boiling mixture of 1,4-dioxane:acetonitrile (8:3 *v/v*) under argon. Afterwards, palladium(II)bis(triphenylphosphane) dichloride (0.01 equiv.) was added to the boiling mixture. The reaction was stirred for 6 h (TLC control: Al₂O₃, F₂₅₄, ethyl acetate:hexane, 1:4). After consumption of the starting materials, the reaction mixture was cooled down to room temperature and water was added. The product was collected by extraction with dichloromethane, and the organic layer was dried with anhydrous MgSO₄. The residue was treated by flash chromatography on silica (ethyl acetate:hexane, 1:2) to remove impurities. The resulting compound was additionally purified by column chromatography on silica using DCM as the eluent to obtain the corresponding *p*-phenyl-6,7-disubstituted naphthalene-2,3-dicarbonitrile.



Scheme 1. Synthesis of 6,7-disubstituted naphthalene-2,3-dicarbonitriles.

3.1.2. Synthesis of 6,7-Bis(4-methoxyphenyl)naphthalene-2,3-dicarbonitrile (OMe)

OMe was synthesized according to the general procedure using **1** (50 mg, 0.15 mmol), 4-methoxyphenylboronic acid (91 mg, 0.6 mmol), and a catalytic amount of palladium(II)bis(triphenylphosphane) dichloride (1 mg, 0.0015 mmol). Molecular formula: C₂₆H₁₈N₂O₂ (pale yellow solid). Yield: 51% (29 mg, 0.07 mmol).

¹H-NMR (500 MHz, DCM-*d*₂): δ (ppm) = 8.37 (s, 2H, 3-*H*), 7.96 (s, 2H, 5-*H*), 7.18–7.12 (m, 4H, 8-*H*), 6.86–6.82 (m, 4H, 9-*H*), 3.80 (s, 6H, 12-*H*).

¹³C-{¹H}-NMR (126 MHz, DCM-*d*₂): δ (ppm) = 159.76 (C-10), 144.47 (C-6), 136.01 (C-3), 132.72 (C-4), 132.54 (C-7), 131.34 (C-8), 130.13 (C-5), 116.69 (C-1), 114.09 (C-9), 110.16 (C-2), 55.65 (C-12).

MS-ESI-EM (CH₂Cl₂, M = C₂₆H₁₈N₂O₂): *m/z* calc. for [M + H]⁺ = 390.13628; found 390.13624 for [M + H]⁺.

3.1.3. Synthesis of 6,7-Bis(4-(dimethylamino)phenyl)naphthalene-2,3-dicarbonitrile (**NMe₂**)

NMe₂ was synthesized according to the general procedure using **1** (50 mg, 0.15 mmol), 4-methoxyphenylboronic acid (98 mg, 0.6 mmol), and a catalytic amount of palladium(II)bis (triphenylphosphane) dichloride (1 mg, 0.0015 mmol). Molecular formula: C₂₈H₂₄N₄ (yellow solid). Yield: 63% (39 mg, 0.09 mmol).

¹H-NMR (400 MHz, DCM-*d*₂): δ (ppm) = 8.30 (s, 2H, 3-*H*), 7.88 (s, 2H, 5-*H*), 7.15–7.09 (m, 4H, 8-*H*), 6.69–6.61 (m, 4H, 9-*H*), 2.96 (s, 12H, 12-*H*).

¹³C-¹H-NMR (101 MHz, DCM-*d*₂): δ (ppm) = 150.36 (C-10), 145.08 (C-6), 135.81 (C-3), 132.55 (C-4), 130.88 (C-8), 129.70 (C-5), 128.09 (C-7), 116.90 (C-1), 112.19 (C-9), 109.49 (C-2), 40.49 (C-12).

MS-ESI-EM (CH₂Cl₂, M = C₂₈H₂₄N₄): *m/z* calcd. for [M + H]⁺ = 417.20737; found 417.20710 for [M + H]⁺.

3.1.4. General Procedure for the Synthesis of Zinc(II) Naphthalocyanines

A mixture of the corresponding 6,7-disubstituted naphthalene-2,3-dicarbonitrile (1 equiv.) and Zn(OAc)₂·2H₂O (0.5 equiv.) was refluxed in 10 mL *i*-amOH (isoamyl alcohol) for 6 h with catalytic amounts of DBU (Figure 1). The reaction mixture was cooled to room temperature, and a MeOH:H₂O mixture (20:1 *v/v*) was added. The precipitate was filtered and washed with a MeOH:H₂O (10:1 *v/v*) mixture. However, the obtained precipitate contained some impurities, which were removed by a Soxhlet extraction with successive solvents of increasing polarity (from diethyl ether to hexane and ethyl acetate). The product was further purified by size exclusion chromatography using a resin (Sephadex-LH20, Amersham Pharmacia Biotech AB, Uppsala, Sweden) in *N,N*-dimethylformamide to obtain the corresponding zinc(II) naphthalocyanines.

3.1.5. Synthesis of 3,4,12,13,21,22,30,31-Octakis(4-methoxyphenyl) Naphthalocyaninato Zinc(II) (**Zn-OMeNc**)

Zn-OMeNc was prepared by treating **OMe** (0.1 g, 0.25 mmol) with Zn(OAc)₂·2H₂O (0.028 g, 0.127 mmol) and using DBU as the catalyst in 10 mL *i*-amOH. The obtained product was precipitated with a MeOH:H₂O (10:1 *v/v*) mixture and filtered. The purification of the obtained products involved a sequential two-step approach. Initially, a Soxhlet extraction was employed using solvents of increasing polarity (from diethyl ether to hexane and ethyl acetate). Subsequently, the resulting product underwent a final purification using size exclusion chromatography with a resin (Sephadex-LH20) in *N,N*-dimethylformamide. The collected fractions were concentrated to obtain the **Zn-OMeNc**. Molecular formula: C₁₀₄H₇₂N₈O₈Zn (brown solid). Yield: 21% (90 mg, 0.05 mmol).

¹H-NMR (400 MHz, DMSO-*d*₆): δ (ppm) = 8.50–8.26 (br, m, 8H, 3-*H*), 8.24–7.97 (br, m, 8H, 5-*H*), 7.15 (m, 16H, 8-*H*), 6.90 (m, 16H, 9-*H*), 3.76 (s, 24H, 11-*H*).

¹³C-¹H-NMR (125 MHz, DMSO-*d*₆): δ (ppm) = 168.80 (C-1), 158.40 (C-10), 141.00 (C-6), 134.10 (C-4), 132.50 (C-7), 131.25 (C-5), 130.70 (C-8), 128.70 (C-2), 123.90 (C-3), 113.54 (C-9), 55.00 (C-11).

MALDI-TOF-MS (CHCl₃, M = C₁₀₄H₇₂N₈O₈Zn): *m/z* calcd. for [M]⁺ = 1624.48; found 1777.51 for [M + 2 Ph]⁺, 1624.40 for [M]⁺, and 1400.36 for [M-2 OMePh]⁺.

3.1.6. Synthesis of 3,4,12,13,21,22,30,31-Octakis(4-(*N,N*-dimethylamino)phenyl) Naphthalocyaninato Zinc(II) (**Zn-NMe₂Nc**)

Zn-NMe₂Nc was prepared by treating **NMe₂** (0.100 g, 0.24 mmol) with Zn(OAc)₂·2H₂O (0.026 g, 0.120 mmol) and using DBU as the catalyst in 10 mL *i*-amOH. The obtained product was precipitated with a MeOH:H₂O (10:1 *v/v*) mixture and filtered. The purification of the obtained products involved a sequential two-step approach. Initially, a Soxhlet extraction was performed using solvents of increasing polarity (from diethyl ether to hexane and ethyl acetate). Subsequently, the resulting product underwent final purification using size exclusion chromatography with a resin (Sephadex-LH20) in *N,N*-dimethylformamide.

The collected fractions were concentrated to obtain the complex **Zn-NMe₂Nc**. Molecular formula: C₁₁₂H₉₆N₁₆Zn (brown solid). Yield: 25% (102.50 mg, 0.06 mmol).

¹H-NMR (400 MHz, DMSO-*d*₆): δ (ppm) = 8.43–8.22 (m, 8H, 3-*H*), 8.14–7.89 (m, 8H, 5-*H*), 7.08 (m, 16H, 8-*H*), 6.65 (m, 16H, 9-*H*), 2.91 (s, 48H, 11-*H*).

¹³C-¹H-NMR (125 MHz, DMSO-*d*₆): δ (ppm) = 168.80 (C-1), 149.10 (C-10), 141.70 (C-6), 133.9 (C-4), 130.90 (C-5), 130.10 (C-8), 128.00 (C-7), 128.0 (C-2), 123.80 (C-3), 111.70 (C-9), 39.90 (C-11).

MALDI-TOF-MS (CHCl₃, M = C₁₁₂H₉₆N₁₆Zn): *m/z* calcd. for [M]⁺ = 1728.73; found 1766.79 for [M + 2H₂O]⁺, 1728.80 for [M]⁺, 1646.71 for [M-NMe₂Ph + 2H₂O]⁺, and 1610.74 for [M-NMe₂Ph]⁺.

3.1.7. Synthesis of 3,4,12,13,21,22,30,31-Octakis(4-(*N,N,N*-trimethylammonium)phenyl)naphthalocyaninato Zinc(II) Octaiodide (**Zn-NMe₃Nc**)

Zn-NMe₃Nc was prepared by treating **Zn-NMe₂Nc** (0.030 g, 0.017 mmol) with methyl iodide (excess) in *N,N*-dimethylformamide for 3 days to quarternize the amino groups (Figure 2). Once the reaction was completed, the desired product was precipitated using acetone and then dried. The compound was further purified with a size exclusion resin (Sephadex-G25, Amersham Pharmacia Biotech AB, Uppsala, Sweden) using water as the eluent. The collected fractions were subjected to lyophilization to obtain **Zn-NMe₃Nc**. Molecular formula: [C₁₂₀H₁₂₀N₁₆Zn]₈ (greenish brown solid). Yield: 87% (28 mg, 0.015 mmol).

¹H-NMR (400 MHz, DMSO-*d*₆): δ (ppm) = 10.08 (s, 8H, 3-*H*), 8.87 (s, 8H, 5-*H*), 8.04 (d, J = 8.6 Hz, 16H, 9-*H*), 7.70 (d, J = 8.4 Hz, 16H, 8-*H*), 3.70 (s, 72H, 11-*H*).

¹³C-¹H-NMR (100 MHz, DMSO-*d*₆): δ (ppm) = 153.48 (C-1), 146.16 (C-10), 142.19 (C-7), 137.35 (C-6), 136.11 (C-2), 132.67 (C-4), 131.59 (C-5), 131.33 (C-8), 121.97 (C-3), 120.31 (C-9), 56.56 (C-11).

MS-ESI-EM (H₂O, M = C₁₂₀H₁₂₀N₁₆Zn⁸⁺): *m/z* calcd. for [M]⁸⁺ = 231.24; found 231.23987 for [M]⁸⁺.

3.1.8. ZnNMe₂Nc Loaded onto Polystyrene Microparticles (PSMPs)

1 μm sized aminated polystyrene microparticles (PSMPs) were bought from Micromod GmbH (Rostock, Germany). The highly hydrophobic complex was encapsulated in the 1 μm sized aminated polystyrene microparticles (PSMPs) via a simple one-step staining procedure as follows: First, 50 mg/mL of PS microparticles were diluted in deionized water to 2.5 mg/mL (1.2 mL). A 0.8 mM solution of the **ZnNMe₂Nc** complex in tetrahydrofuran (THF) was prepared. Then, 200 μL of this solution in THF was added to the PSMP dispersion in water, and the sample was subsequently shaken for 40 min. Shrinkage of the particles was induced by adding 200 μL of deionized water to the dispersion, thereby encapsulating the complex in the microparticles. The particles were then centrifuged at 16,000 rpm for 5 min (Megafuge™ 16 from Thermo Scientific, Schwerte, Germany). The precipitate was washed three times with ethanol/water mixtures (volume ratios of 40/60, 30/70, and 20/80) and once with deionized water to remove the excess of dye that was adsorbed onto the particles' surface. Finally, the suspension containing the PSMPs loaded with the **ZnNMe₂Nc** complex was diluted to 5 mg/mL (600 μL).

3.2. NMR Spectroscopy and Mass Spectrometry

NMR spectra were obtained at the Institut für Anorganische und Analytische Chemie (Universität Münster), using Bruker Avance Neo 500 and Bruker Avance III 400. All measurements were performed at room temperature unless otherwise specified. The ¹H-NMR and ¹³C-NMR chemical shifts (δ) of the signals are given in parts per million and are referenced to the residual proton signal in the deuterated solvent DCM-*d*₂ (¹H: 5.32 ppm/¹³C: 54.0 ppm) or DMSO-*d*₆ (¹H: 2.50 ppm/¹³C: 39.52 ppm). The signal multiplicities are abbreviated as follows: s, singlet; d, doublet; t, triplet; q, quartet; br, broad; m, multiplet.

Exact mass (EM) determination by mass spectrometry (MS) was carried out at the Organisch-Chemisches Institut (Universität Münster) using a LTQ Orbitrap LTQ XL (Thermo-Fisher Scientific, Bremen, Germany) with electrospray ionization (ESI). MALDI-TOF mass spectra were taken on Autoflex Speed MALDI-TOF spectrometer with 2-[(2E)-3-(4-*tert*-butylphenyl)-2-methylprop-2-enylidene]malonitrile (DCTB) as the matrix.

3.3. Absorption and Fluorescence Spectroscopy

Absorption spectra were measured using quartz Hellma[®] (Müllheim, Germany) square cuvettes on a Shimadzu UV-3600i Plus UV-vis-NIR spectrophotometer (Shimadzu, Kyoto, Japan) and baseline-corrected.

Steady-state excitation and emission spectra were recorded on a FluoTime 300 spectrometer from PicoQuant (Berlin, Germany), equipped with a 300 W ozone-free Xe lamp (250–900 nm), a 10 W Xe flash lamp (250–900 nm, pulse width < 10 μ s) with repetition rates of 0.1–300 Hz, a single-grating excitation monochromator (Czerny-Turner 2.7 nm/mm dispersion, 1200 grooves/mm, blazed at 300 nm), diode lasers (pulse width < 80 ps) operated by a computer-controlled laser driver PDL-820 (repetition rate up to 80 MHz, burst mode for slow and weak decays), two single-grating emission monochromators (Czerny-Turner, selectable gratings blazed at 500 nm with 2.7 nm/mm dispersion and 1200 grooves/mm, or blazed at 1250 nm with 5.4 nm/mm dispersion and 600 grooves/mm), Glan-Thompson polarizers for excitation (Xe-lamps) and emission, a Peltier-thermostatized sample holder from Quantum Northwest (Washington, DC, USA) (−40–105 °C), and two detectors, namely, a PMA Hybrid 40 (transit time spread FWHM < 120 ps, 300–720 nm) and a R5509-42 NIR photomultiplier tube (transit time spread FWHM 1.5 ns, 300–1400 nm) with external cooling (−80 °C) from Hamamatsu (Shizuoka, Japan). Steady-state and fluorescence lifetimes were recorded in the TCSPC mode by a PicoHarp 300 (minimum base resolution 4 ps) from PicoQuant (Berlin, Germany). Emission and excitation spectra were corrected for source intensity (lamp and grating) by standard correction curves. Lifetime analysis was performed using the commercial EasyTau software (version 2.2) package from PicoQuant (Berlin, Germany). The quality of the fit was assessed by minimizing the reduced chi squared function (χ^2) and through visual inspection of the weighted residuals and their autocorrelation. At least three independent batches of the compounds were synthesized and measured, with the samples undergoing multiple measurements to ensure data consistency and to mitigate measurement errors. Across these different batches, the results were consistently identical, underscoring the reliability of our findings.

3.4. Computational Details

All density functional theory (DFT) and time-dependent density functional theory (TD-DFT) calculations were performed using the quantum chemistry package Gaussian 09 Rev. D.01 [80]. Geometry optimizations in the ground state S_0 were carried out with DFT, while TD-DFT was employed to obtain the optimized S_1 and S_3 excited state structures. The solvent dimethyl sulfoxide (DMSO) was modelled by the polarizable continuum model (PCM) in an integral equation formalism framework [81] with atomic radii from the universal force field model (UFF) [82]. In all cases, the spectral properties were calculated using the same functional as employed for geometry optimization.

UV-vis absorption spectra were calculated using the B3LYP functional [83], along with Grimme's D3 dispersion correction with Becke–Johnson damping (BJ) [84] and the SDD basis set, which applies an effective core potential for the Zn atom [85] and the D95 basis set for H, C, N, and O atoms [86]. For each absorption spectrum, the 120 lowest excited singlet states were considered. A Lorentzian broadening with a half width of half maximum (HWHM) of 30 nm was used for each transition.

The emission wavelengths were obtained from the difference in energy between the optimized ground state and the corresponding excited state geometries (0-0). In addition to the B3LYP functional, emission spectra were also calculated with the CAM-B3LYP [87], PBE0 [88], and M06-2X [89] functionals due to the delicate balance between local and charge-transfer excitations. A Lorentzian broadening with a half width of half maximum

(HWHM) of 20 nm was used for the $S_1 \rightarrow S_0$ transition, while a value of 60 nm was applied for the $S_3 \rightarrow S_0$ transition to match the experimental line shape.

3.5. MSOT Photoacoustic Imaging

Phantom photoacoustic imaging experiments were performed using a Multispectral Optoacoustic Tomography system (MSOT inVision 512-echo, iThera Medical, Munich, Germany). The phantom consists of a cylinder of 1.5% agarose with 2% of 20% soybean cream as scattering medium and 0.75% 2.5 mM Nigrosin, which was cast, including 2 straws as placeholders. Once hardened, these placeholders were removed and replaced with sealed straws, which had been filled with test solution and a control containing only the solvent. Multispectral photoacoustic imaging of phantoms containing the probe and control samples were performed tomographically for the length of the straw using an excitation wavelength ranging from 680 to 900 nm in steps of 5 nm. Images were loaded into an in-house developed image processing software, MEDgical (Version 0.9.9, EIMI, Münster, Germany). Spectra were exported and processed to create the presented plots.

3.6. Fluorescence Lifetime Imaging Microscopy (FLIM) by Time-Resolved Multiphoton Micro(spectro)scopy

Fluorescence lifetime imaging microscopy (FLIM) was recorded on a fluorescence microscope IX 73 from Olympus (Shinjuku, Japan) with a complete confocal system and a laser-combining unit (LCU), an inverted microscope body, and a multichannel detection unit, namely a MicroTime 200 from PicoQuant (Berlin, Germany) equipped with diode lasers (providing adjustable output power and repetition rates up to 80 MHz inside a compact fiber couple unit with wavelengths between 375 and 900 nm). For beam diagnostics, a charge-coupled device (CCD) camera and a photodiode were available in the main optical unit (MOU) of the microscope. The MOU was equipped with two detectors, namely, a hybrid photomultiplier-based single photon counting module (PMA Hybrid 40, PicoQuant) and an SPAD-based photon-counting module (SPCM-AQR-14, Perkin-Elmer, Hopkinton, MA, USA). Different band-pass (BP) and low-pass (LP) filters were placed before these detectors on demand to acquire lifetime maps. Data acquisition was based on the unique time-tagged time-resolved (TTTR) measurement mode, where simultaneous data acquisition on two channels is possible. Data were processed and analyzed with the SymphoTime 64 (PicoQuant) software. In order to couple the MicroTime 200 and the FluoTime 300 instruments (both from PicoQuant, Berlin, Germany), a fiber coupler was employed. In this way, the spectrometer can be used to record either steady-state or time-resolved luminescence spectra and decays from a sample mounted on the microscope. Luminescence micrographs were acquired using the same microscope mentioned above, equipped with an X-CiteQ Lamp module (Excelitas Technologies, Waltham, MA, USA) as excitation source and a UI-5580SE (IDS) digital camera. Different band-pass (BP) and low-pass (LP) cubes were using accordingly.

Additionally, a two-photon (Mai Tai[®] from SpectraPhysics, Darmstadt, Germany) Ti:Sapphire laser (Ti:Sa oscillator) with a pulse with <100 fs and tuning range of 690–1040 nm, connected to the MOU, can be used as excitation source. In order to reduce the repetition rate, the Ti:Sapphire laser was connected to a double pulse picker (A.P.E.[®], Berlin, Germany).

4. Conclusions

In conclusion, we report on a set of novel Zn(II) naphthalocyaninates with a prominent dual fluorescence encompassing the visible and the NIR portion of the electromagnetic spectrum. A proper synthesis, purification, and full characterization of the peripherally octa-substituted zinc(II) naphthalocyaninato complexes **Zn-OMeNc**, **Zn-NMe₂Nc**, and **Zn-NMe₃Nc** was undertaken for the first time; hence, a detailed structural elucidation based on NMR studies is provided. The introduction of a push-pull system on the macrocycle enabled the integration of two orthogonal chromophores with unprecedented dual emission, which was assigned by means of TD-DFT calculations. Upon quaternization of

Zn-NMe₂Nc, we produced the first to-date reported octa-cationic water-soluble zinc(II) naphthalocyaninate, namely, **Zn-NMe₃Nc**. The quaternized species, **Zn-NMe₃Nc**, exhibited excellent solubility in water; even though aggregation phenomena can be traced in aqueous media, stacking is suppressed in DMSO. Furthermore, due to its good absorption in the near-infrared region, we also investigated the photoacoustic imaging capability of **Zn-NMe₂Nc** and **Zn-NMe₃Nc**. The photoacoustic profiles of these Ncs, studied in gel phantoms, show a high intensity and red-shifted photoacoustic maxima in a broad concentration range. Among **Zn-NMe₂Nc** and **Zn-NMe₃Nc**, the best photoacoustic performance was observed for **Zn-NMe₃Nc** in DMSO, particularly in terms of its detectability at lower concentrations. Staining microparticles with **Zn-NMe₂Nc** revealed that the additional readout in the visible range stemming from the side groups enables time-resolved multiphoton micro(spectro)scopy. This holds true even when aggregation quenches the intrinsic fluorescence of the macrocycle. Since well-defined purification and characterization techniques for Ncs are sparsely found in the literature, this work could expand the possibilities of water-soluble dyes for PDT and diagnostics. More generally, the unprecedented dual emission (visible and NIR) unlocks the prospective use of naphthalocyanines for multiscale–multimodal bioimaging and for applications in sensing or optoelectronics.

Supplementary Materials: The following supporting information can be downloaded at: <https://www.mdpi.com/article/10.3390/ijms25052605/s1>.

Author Contributions: Conceptualization, S.T.N.S., I.M., A.F. and C.A.S.; methodology, S.T.N.S., I.M., N.L.D. and C.A.S.; validation, S.T.N.S., I.M., A.F., N.L.D. and C.A.S.; formal analysis, S.T.N.S., I.M., A.F., D.B., N.L.D., S.H. and C.A.S.; investigation, S.T.N.S., I.M., D.B., N.L.D. and S.H.; resources, N.L.D. and C.A.S.; NMR-measurements, A.H.; NMR-structure analysis, A.H. and S.T.N.S.; data curation, S.T.N.S. and I.M.; writing—original draft preparation, S.T.N.S. and I.M.; writing—review and editing, S.T.N.S., I.M., A.F., D.B., N.L.D. and C.A.S.; visualization, S.T.N.S., I.M., D.B. and N.L.D.; supervision, A.F., N.L.D. and C.A.S.; project administration, N.L.D. and C.A.S.; funding acquisition, N.L.D. and C.A.S. All authors have read and agreed to the published version of the manuscript.

Funding: C.A.S. and A.F. gratefully acknowledge the CRC 1450-431,460,824 (SFB “inSight”, projects A02 and A03), both funded by the DFG. C.A.S. would also like to acknowledge the DFG (EXC 1003 Cluster of Excellence “Cells in Motion”), as well as DFG/Land NRW (INST 211/915-1 FUGG: “Integrated confocal luminescence spectrometer with spatiotemporal resolution and multiphoton excitation”), for generous financial support. S.T.N.S. thank the generous research funding from DAAD (Deutscher Akademischer Austauschdienst) for the doctoral fellowship. N.L.D. thanks DFG for funding (DO 768/5-1).

Institutional Review Board Statement: Not applicable.

Informed Consent Statement: Not applicable.

Data Availability Statement: The data that support the findings of this study are available in the Supplementary Material of this article.

Acknowledgments: The authors would like to thank Uwe Karst and Michael Holtkamp for assistance in determining the concentration of Zn by TXRF and Sarah Köster for MSOT photoacoustic imaging, supported by the Interdisciplinary Center for Clinical Research (IZKF core unit PIX), Münster, Germany.

Conflicts of Interest: The authors declare no conflict of interest.

References

1. Kukhta, N.A.; Bryce, M.R. Dual Emission in Purely Organic Materials for Optoelectronic Applications. *Mater. Horiz.* **2021**, *8*, 33–55. [[CrossRef](#)] [[PubMed](#)]
2. Sung, R.; Sung, K. TICT Excited States of *o*- and *p*-*N,N*-Dimethylamino Analogues of GFP Chromophore. *J. Phys. Org. Chem.* **2018**, *31*, e3791. [[CrossRef](#)]
3. Lippert, E.; Lüder, W.; Moll, F.; Nägele, W.; Boos, H.; Prigge, H.; Seibold-Blankenstein, I. Umwandlung von Elektronenanregungsenergie. *Angew. Chem.* **1961**, *73*, 695–706. [[CrossRef](#)]

4. Atsbeha, T.; Mohammed, A.M.; Redi-Abshiro, M. Excitation Wavelength Dependence of Dual Fluorescence of DMABN in Polar Solvents. *J. Fluoresc.* **2010**, *20*, 1241–1248. [[CrossRef](#)]
5. Chou, P.-T.; Pu, S.-C.; Cheng, Y.-M.; Yu, W.-S.; Yu, Y.-C.; Hung, F.-T.; Hu, W.-P. Femtosecond Dynamics on Excited-State Proton/Charge-Transfer Reaction in 4'-N,N-Diethylamino-3-Hydroxyflavone. The Role of Dipolar Vectors in Constructing a Rational Mechanism. *J. Phys. Chem. A* **2005**, *109*, 3777–3787. [[CrossRef](#)] [[PubMed](#)]
6. Ma, L.-H.; Chen, Z.-B.; Jiang, Y.-B. Intramolecular Charge Transfer with 4-(N-Phenylamino)Benzoic Acid. The N-Phenyl Amino Conjugation Effect. *Chem. Phys. Lett.* **2003**, *372*, 104–113. [[CrossRef](#)]
7. Murali, S.; Rettig, W. TICT Formation in Para- and Meta-Derivatives of N-Phenylpyrrole. *J. Phys. Chem. A* **2006**, *110*, 28–37. [[CrossRef](#)]
8. Pereira, R.V.; Garcia Ferreira, A.P.; Gehlen, M.H. Excited-State Intramolecular Charge Transfer in 9-Aminoacridine Derivative. *J. Phys. Chem. A* **2005**, *109*, 5978–5983. [[CrossRef](#)]
9. Bag, S.S.; Kundu, R. Sensing of Micellar Microenvironment with Dual Fluorescent Probe, Triazolylpyrene (TNDMBPy). *J. Fluoresc.* **2013**, *23*, 929–938. [[CrossRef](#)]
10. Etaiw, S.E.-D.H.; Fayed, T.A.; Saleh, N.Z. Photophysics of Benzazole Derived Push–Pull Butadienes: A Highly Sensitive Fluorescence Probes. *J. Photochem. Photobiol. A Chem.* **2006**, *177*, 238–247. [[CrossRef](#)]
11. Chen, K.-Y.; Tsai, H.-Y. Synthesis, X-Ray Structure, Spectroscopic Properties and DFT Studies of a Novel Schiff Base. *Int. J. Mol. Sci.* **2014**, *15*, 18706–18724. [[CrossRef](#)]
12. Gómez, I.; Mercier, Y.; Reguero, M. Theoretical Investigation of Luminescence Behavior as a Function of Alkyl Chain Size in 4-Aminobenzonitrile Alicyclic Derivatives. *J. Phys. Chem. A* **2006**, *110*, 11455–11461. [[CrossRef](#)]
13. Lippert, E.; Lüder, W.; Boos, H. Advances in Molecular Spectroscopy. In *Proceedings of the European Conference on Molecular Spectroscopy, Bologna, Italy, 1959*; Macmillan: New York, NY, USA, 1962; Volume 2.
14. Bosshard, C. *Organic Nonlinear Optical Materials*; CRC Press: Boca Raton, FL, USA, 2020; ISBN 0429114095.
15. Kippelen, B.; Lackritz, H.S.; Claus, R.O. *Organic Nonlinear Optical Materials and Devices: Symposium Held 6–9 April 1999, San Francisco, CA, USA*; Materials Research Society: Warrendale, PA, USA, 1999; ISBN 1558994688.
16. Zhang, Y.; Lovell, J.F. Recent Applications of Phthalocyanines and Naphthalocyanines for Imaging and Therapy. *WIREs Nanomed. Nanobiotechnol.* **2017**, *9*, e1420. [[CrossRef](#)]
17. Santos, K.L.M.; Barros, R.M.; da Silva Lima, D.P.; Nunes, A.M.A.; Sato, M.R.; Faccio, R.; de Lima Damasceno, B.P.G.; Oshiro-Junior, J.A. Prospective Application of Phthalocyanines in the Photodynamic Therapy against Microorganisms and Tumor Cells: A Mini-Review. *Photodiagn. Photodyn. Ther.* **2020**, *32*, 102032. [[CrossRef](#)]
18. Schmidt, A.M.; Calvete, M.J.F. Phthalocyanines: An Old Dog Can Still Have New (Photo)Tricks! *Molecules* **2021**, *26*, 2823. [[CrossRef](#)] [[PubMed](#)]
19. Dubinina, T.V.; Moiseeva, E.O.; Astvatsaturov, D.A.; Borisova, N.E.; Tarakanov, P.A.; Trashin, S.A.; De Wael, K.; Tomilova, L.G. Novel 2-Naphthyl Substituted Zinc Naphthalocyanine: Synthesis, Optical, Electrochemical and Spectroelectrochemical Properties. *New J. Chem.* **2020**, *44*, 7849–7857. [[CrossRef](#)]
20. Leem, D.-S.; Lee, K.-H.; Li, N.; Park, B.W.; Choi, T.; Ro, T.; Kwon, O.K.; Kwon, Y.-N.; Ng, T.N.; Kim, S. Highly Responsive and Thermally Reliable Near-Infrared Organic Photodiodes Utilizing Naphthalocyanine Molecules Tuned with Axial Ligands. *Adv. Opt. Mater.* **2021**, *9*, 2001682. [[CrossRef](#)]
21. Taratula, O.; Doddapaneni, B.S.; Schumann, C.; Li, X.; Bracha, S.; Milovancev, M.; Alani, A.W.G.; Taratula, O. Naphthalocyanine-Based Biodegradable Polymeric Nanoparticles for Image-Guided Combinatorial Phototherapy. *Chem. Mater.* **2015**, *27*, 6155–6165. [[CrossRef](#)]
22. Huang, H.; Wang, D.; Zhang, Y.; Zhou, Y.; Geng, J.; Chitgupi, U.; Cook, T.R.; Xia, J.; Lovell, J.F. Axial PEGylation of Tin Octabutoxy Naphthalocyanine Extends Blood Circulation for Photoacoustic Vascular Imaging. *Bioconjug. Chem.* **2016**, *27*, 1574–1578. [[CrossRef](#)]
23. Dubinina, T.V.; Trashin, S.A.; Borisova, N.E.; Boginskaya, I.A.; Tomilova, L.G.; Zefirov, N.S. Phenyl-Substituted Planar Binuclear Phthalo- and Naphthalocyanines: Synthesis and Investigation of Physicochemical Properties. *Dye. Pigment.* **2012**, *93*, 1471–1480. [[CrossRef](#)]
24. Dubinina, T.V.; Kosov, A.D.; Petrusevich, E.F.; Borisova, N.E.; Trigub, A.L.; Mamin, G.V.; Gilmutdinov, I.F.; Masitov, A.A.; Tokarev, S.V.; Pushkarev, V.E.; et al. Sandwich Double-Decker Er(III) and Yb(III) Complexes Containing Naphthalocyanine Moiety: Synthesis and Investigation of the Effect of a Paramagnetic Metal Center. *Dalton Trans.* **2019**, *48*, 13413–13422. [[CrossRef](#)]
25. Dubinina, T.V.; Tychinsky, P.I.; Borisova, N.E.; Maklakov, S.S.; Sedova, M.V.; Kosov, A.D.; Tomilova, L.G.; Zefirov, N.S. Zinc Complexes of 3-(Ethylthio)Phenyl-Substituted Phthalocyanines and Naphthalocyanine: Synthesis and Investigation of Physicochemical Properties. *Dye. Pigment.* **2017**, *144*, 41–47. [[CrossRef](#)]
26. Dubinina, T.V.; Paramonova, K.V.; Trashin, S.A.; Borisova, N.E.; Tomilova, L.G.; Zefirov, N.S. Novel Near-IR Absorbing Phenyl-Substituted Phthalo- and Naphthalocyanine Complexes of Lanthanide(III): Synthesis and Spectral and Electrochemical Properties. *Dalton Trans.* **2014**, *43*, 2799–2809. [[CrossRef](#)] [[PubMed](#)]
27. Saad, M.A.; Pawle, R.; Selfridge, S.; Contreras, L.; Xavierselvan, M.; Nguyen, C.D.; Mallidi, S.; Hasan, T. Optimizing Axial and Peripheral Substitutions in Si-Centered Naphthalocyanine Dyes for Enhancing Aqueous Solubility and Photoacoustic Signal Intensity. *Int. J. Mol. Sci.* **2023**, *24*, 2241. [[CrossRef](#)] [[PubMed](#)]

28. Vagin, S.; Hanack, M. Synthesis and Characterization of Soluble Octaaryl- and Octaaryloxy-Substituted Metal-Naphthalocyanines. *Eur. J. Org. Chem.* **2003**, *2003*, 2661–2669. [[CrossRef](#)]
29. Luan, L.; Ding, L.; Zhang, W.; Shi, J.; Yu, X.; Liu, W. A Naphthalocyanine Based Near-Infrared Photosensitizer: Synthesis and in vitro Photodynamic Activities. *Bioorg. Med. Chem. Lett.* **2013**, *23*, 3775–3779. [[CrossRef](#)] [[PubMed](#)]
30. Mitra, K.; Hartman, M.C.T. Silicon Phthalocyanines: Synthesis and Resurgent Applications. *Org. Biomol. Chem.* **2021**, *19*, 1168–1190. [[CrossRef](#)]
31. Kakade, S.; Ghosh, R.; Palit, D.K. Excited State Dynamics of Zinc-Phthalocyanine Nanoaggregates in Strong Hydrogen Bonding Solvents. *J. Phys. Chem. C* **2012**, *116*, 15155–15166. [[CrossRef](#)]
32. Safonova, E.A.; Polovkova, M.A.; Martynov, A.G.; Gorbunova, Y.G.; Tsivadze, A.Y. Crown-Substituted Naphthalocyanines: Synthesis and Supramolecular Control over Aggregation and Photophysical Properties. *Dalton Trans.* **2018**, *47*, 15226–15231. [[CrossRef](#)]
33. de Souza, T.; Antonio, F.; Zanotto, M.; Homem-de-Mello, P.; Ribeiro, A. Photophysical and Photochemical Properties and Aggregation Behavior of Phthalocyanine and Naphthalocyanine Derivatives. *J. Braz. Chem. Soc.* **2017**, *29*, 1199–1209. [[CrossRef](#)]
34. Dubinina, T.V.; Maklakov, S.S.; Petrusevich, E.F.; Borisova, N.E.; Trashin, S.A.; De Wael, K.; Tomilova, L.G. Photoactive Layers for Photovoltaics Based on Near-Infrared Absorbing Aryl-Substituted Naphthalocyanine Complexes: Preparation and Investigation of Properties. *New J. Chem.* **2021**, *45*, 14815–14821. [[CrossRef](#)]
35. Dubinina, T.V.; Borisova, N.E.; Paramonova, K.V.; Tomilova, L.G. Synthesis and Spectral Properties of Dodecaphenyl-Substituted Planar Binuclear Naphthalocyanine Magnesium Complex Sharing a Common Benzene Ring. *Mendeleev Commun.* **2011**, *21*, 165–167. [[CrossRef](#)]
36. Keleş, T.; Barut, B.; Özel, A.; Biyiklioglu, Z. Design, Synthesis and Biological Evaluation of Water Soluble and Non-Aggregated Silicon Phthalocyanines, Naphthalocyanines against A549, SNU-398, SK-MEL128, DU-145, BT-20 and HFC Cell Lines as Potential Anticancer Agents. *Bioorg. Chem.* **2021**, *107*, 104637. [[CrossRef](#)] [[PubMed](#)]
37. Biyiklioglu, Z.; Alp, H. Synthesis and Electropolymerization Studies of Non-Aggregated (4-{3-[3-(Dimethylamino,diethylamino)phenoxy]propoxy}phenyl)propanoxy Substituted Silicon Naphthalocyanines. *J. Coord. Chem.* **2017**, *70*, 2359–2370. [[CrossRef](#)]
38. Wheeler, B.L.; Nagasubramanian, G.; Bard, A.J.; Schechtman, L.A.; Kenney, M.E. A Silicon Phthalocyanine and a Silicon Naphthalocyanine: Synthesis, Electrochemistry, and Electrogenerated Chemiluminescence. *J. Am. Chem. Soc.* **1984**, *106*, 7404–7410. [[CrossRef](#)]
39. Sato, K.; Ando, K.; Okuyama, S.; Moriguchi, S.; Ogura, T.; Totoki, S.; Hanaoka, H.; Nagaya, T.; Kokawa, R.; Takakura, H.; et al. Photoinduced Ligand Release from a Silicon Phthalocyanine Dye Conjugated with Monoclonal Antibodies: A Mechanism of Cancer Cell Cytotoxicity after Near-Infrared Photoimmunotherapy. *ACS Cent. Sci.* **2018**, *4*, 1559–1569. [[CrossRef](#)] [[PubMed](#)]
40. Choi, H.; Choi, W.; Kim, J.; Kong, W.H.; Kim, K.S.; Kim, C.; Hahn, S.K. Multifunctional Nanodroplets Encapsulating Naphthalocyanine and Perfluorohexane for Bimodal Image-Guided Therapy. *Biomacromolecules* **2019**, *20*, 3767–3777. [[CrossRef](#)] [[PubMed](#)]
41. Marchenko, I.V.; Borodina, T.N.; Trushina, D.B.; Nabatov, B.V.; Logachev, V.V.; Plotnikov, G.S.; Baranov, A.N.; Saletskii, A.M.; Ryabova, A.V.; Bukreeva, T.V. Incorporation of Naphthalocyanine into Shells of Polyelectrolyte Capsules and Their Disruption under Laser Radiation. *Colloid J.* **2018**, *80*, 399–406. [[CrossRef](#)]
42. Li, H.; Jensen, T.J.; Fronczek, F.R.; Vicente, M.G.H. Syntheses and Properties of a Series of Cationic Water-Soluble Phthalocyanines. *J. Med. Chem.* **2008**, *51*, 502–511. [[CrossRef](#)]
43. Huang, J.-D.; Wang, S.; Lo, P.-C.; Fong, W.-P.; Ko, W.-H.; Ng, D.K.P. Halogenated Silicon(IV) Phthalocyanines with Axial Poly(Ethylene Glycol) Chains. Synthesis, Spectroscopic Properties, Complexation with Bovine Serum Albumin and in vitro Photodynamic Activities. *New J. Chem.* **2004**, *28*, 348–354. [[CrossRef](#)]
44. Lo, P.-C.; Huang, J.-D.; Cheng, D.Y.Y.; Chan, E.Y.M.; Fong, W.-P.; Ko, W.-H.; Ng, D.K.P. New Amphiphilic Silicon(IV) Phthalocyanines as Efficient Photosensitizers for Photodynamic Therapy: Synthesis, Photophysical Properties, and in vitro Photodynamic Activities. *Chem.—A Eur. J.* **2004**, *10*, 4831–4838. [[CrossRef](#)]
45. Lee, P.P.S.; Lo, P.-C.; Chan, E.Y.M.; Fong, W.-P.; Ko, W.-H.; Ng, D.K.P. Synthesis and in vitro Photodynamic Activity of Novel Galactose-Containing Phthalocyanines. *Tetrahedron Lett.* **2005**, *46*, 1551–1554. [[CrossRef](#)]
46. Huang, J.-D.; Lo, P.-C.; Chen, Y.-M.; Lai, J.C.; Fong, W.-P.; Ng, D.K.P. Preparation and in vitro Photodynamic Activity of Novel Silicon(IV) Phthalocyanines Conjugated to Serum Albumins. *J. Inorg. Biochem.* **2006**, *100*, 946–951. [[CrossRef](#)]
47. Liu, W.; Jensen, T.J.; Fronczek, F.R.; Hammer, R.P.; Smith, K.M.; Vicente, M.G.H. Synthesis and Cellular Studies of Nonaggregated Water-Soluble Phthalocyanines. *J. Med. Chem.* **2005**, *48*, 1033–1041. [[CrossRef](#)]
48. Yang, Y.C.; Ward, J.R.; Seiders, R.P. Dimerization of Cobalt(II) Tetrasulfonated Phthalocyanine in Water and Aqueous Alcoholic Solutions. *Inorg. Chem.* **1985**, *24*, 1765–1769. [[CrossRef](#)]
49. Oleinick, N.L.; Antunez, A.R.; Clay, M.E.; Rihter, B.D.; Kenney, M.E. New Phthalocyanine Photosensitizers for Photodynamic Therapy. *Photochem. Photobiol.* **1993**, *57*, 242–247. [[CrossRef](#)]
50. Li, Y.-S.; Zaidi, S.I.A.; Rodgers, M.A.J.; Mukhtar, H.; Kenney, M.E.; Oleinick, N.L.; He, J.; Larkin, H.E.; Rihter, B.D. The Synthesis, Photophysical and Photobiological Properties and in vitro Structure-Activity Relationships of a Set of Silicon Phthalocyanine PDT Photosensitizers. *Photochem. Photobiol.* **1997**, *65*, 581–586. [[CrossRef](#)]

51. Lee, P.P.S.; Ngai, T.; Huang, J.-D.; Wu, C.; Fong, W.-P.; Ng, D.K.P. Synthesis, Characterization, Biodegradation, and in vitro Photodynamic Activities of Silicon(IV) Phthalocyanines Conjugated Axially with Poly(ϵ -Caprolactone). *Macromolecules* **2003**, *36*, 7527–7533. [[CrossRef](#)]
52. Lee, P.P.S.; Ngai, T.; Yang, C.; Wu, C.; Ng, D.K.P. Synthesis, Characterization, and Degradation of Silicon(IV) Phthalocyanines Conjugated Axially with Poly(sebacic anhydride). *J. Polym. Sci. Part A Polym. Chem.* **2005**, *43*, 837–843. [[CrossRef](#)]
53. Zhu, Y.-J.; Huang, J.-D.; Jiang, X.-J.; Sun, J.-C. Novel Silicon Phthalocyanines Axially Modified by Morpholine: Synthesis, Complexation with Serum Protein and in vitro Photodynamic Activity. *Inorg. Chem. Commun.* **2006**, *9*, 473–477. [[CrossRef](#)]
54. Wöhrle, D.; Iskander, N.; Grashew, G.; Sinn, H.; Friedrich, E.A.; Maier-Borst, W.; Stern, J.; Schlag, P. Synthesis of Positively Charged Phthalocyanines and Their Activity in the Photodynamic Therapy of Cancer Cells. *Photochem. Photobiol.* **1990**, *51*, 351–356. [[CrossRef](#)]
55. Michelsen, U.; Schnurpfeil, G.; Sobbi, A.K.; Wöhrle, D.; Kliesch, H. Unsymmetrically Substituted Benzonaphthoporphyrines: A New Class of Cationic Photosensitizers for the Photodynamic Therapy of Cancer*. *Photochem. Photobiol.* **1996**, *64*, 694–701. [[CrossRef](#)]
56. Sobbi, A.K.; Wöhrle, D.; Schlettwein, D. Photochemical Stability of Various Porphyrins in Solution and as Thin Film Electrodes. *J. Chem. Soc. Perkin Trans.* **1993**, *2*, 481–488. [[CrossRef](#)]
57. Brewis, M.; Helliwell, M.; McKeown, N.B. Phthalocyanine-Centred and Naphthalocyanine-Centred Aryl Ether Dendrimers with Oligo(Ethyleneoxy) Surface Groups. *Tetrahedron* **2003**, *59*, 3863–3872. [[CrossRef](#)]
58. Lioret, V.; Saou, S.; Berrou, A.; Lernerman, L.; Arnould, C.; Décréau, R.A. Water Soluble Octa-Imidazolium Zinc Phthalocyanine for Nucleus/Nucleolus Cell Fluorescence Microscopy and Photodynamic Therapy. *Photochem. Photobiol. Sci.* **2023**, *22*, 303–309. [[CrossRef](#)]
59. Iqbal, Z.; Lyubimtsev, A.; Hanack, M.; Ziegler, T. Anomerically Glycosylated Zinc(II) Naphthalocyanines. *Tetrahedron Lett.* **2009**, *50*, 5681–5685. [[CrossRef](#)]
60. Thulaseedharan Nair Sailaja, S.; Maisuls, I.; Kösters, J.; Hepp, A.; Faust, A.; Voskuhl, J.; Strassert, C.A. Naphthalonitriles Featuring Efficient Emission in Solution and in the Solid State. *Beilstein J. Org. Chem.* **2020**, *16*, 2960–2970. [[CrossRef](#)]
61. Esenpinar, A.A.; Bulut, M. Synthesis and Characterization of Novel α - or β -Tetra[6,7-dihexyloxy-3-(4-oxyphenyl)coumarin]-Substituted Metal-Free and Metallo Phthalocyanines. *Polyhedron* **2009**, *28*, 3129–3137. [[CrossRef](#)]
62. Biyikloğlu, Z.; Kantekin, H. Synthesis and Spectroscopic Properties of a Series of Octacationic Water-Soluble Phthalocyanines. *Synth. Met.* **2011**, *161*, 943–948. [[CrossRef](#)]
63. Ghazal, B.; Azizi, K.; Ewies, E.F.; Youssef, A.S.A.; Mwalukuku, V.M.; Demadrille, R.; Torres, T.; Makhseed, S. Push–Pull Zinc Phthalocyanine Bearing Hexa-Tertiary Substituted Carbazolyl Donor Groups for Dye-Sensitized Solar Cells. *Molecules* **2020**, *25*, 1692. [[CrossRef](#)] [[PubMed](#)]
64. Ince, M.; Cardinali, F.; Yum, J.-H.; Martínez-Díaz, M.V.; Nazeeruddin, M.K.; Grätzel, M.; Torres, T. Convergent Synthesis of Near-Infrared Absorbing, “Push–Pull”, Bisthiophene-Substituted, Zinc(II) Phthalocyanines and Their Application in Dye-Sensitized Solar Cells. *Chem.—A Eur. J.* **2012**, *18*, 6343–6348. [[CrossRef](#)]
65. Kazak, A.V.; Marchenkova, M.A.; Dubinina, T.V.; Smirnova, A.I.; Tomilova, L.G.; Rogachev, A.V.; Chausov, D.N.; Stsiapanau, A.A.; Usol'tseva, N.V. Self-Organization of Octa-Phenyl-2,3-Naphthalocyaninato Zinc Floating Layers. *New J. Chem.* **2020**, *44*, 3833–3837. [[CrossRef](#)]
66. Kutlu, Ö.D.; Avcil, D.; Erdoğan, A. New Water-Soluble Cationic Indium (III) Phthalocyanine Bearing Thioquinoline Moiety; Synthesis, Photophysical and Photochemical Studies with High Singlet Oxygen Yield. *Main Group Chem.* **2019**, *18*, 139–151. [[CrossRef](#)]
67. Strassert, C.A.; Bilmes, G.M.; Awruch, J.; Dico, L.E. Comparative Photophysical Investigation of Oxygen and Sulfur as Covalent Linkers on Octaalkylamino Substituted Zinc(II) Phthalocyanines. *Photochem. Photobiol. Sci.* **2008**, *7*, 738–747. [[CrossRef](#)] [[PubMed](#)]
68. Bézière, N.; Ntziachristos, V. Optoacoustic Imaging of Naphthalocyanine: Potential for Contrast Enhancement and Therapy Monitoring. *J. Nucl. Med.* **2015**, *56*, 323–328. [[CrossRef](#)] [[PubMed](#)]
69. Duffy, M.J.; Planas, O.; Faust, A.; Vogl, T.; Hermann, S.; Schäfers, M.; Nonell, S.; Strassert, C.A. Towards Optimized Naphthalocyanines as Sonochromes for Photoacoustic Imaging in vivo. *Photoacoustics* **2018**, *9*, 49–61. [[CrossRef](#)] [[PubMed](#)]
70. Liu, N.; Gujrati, V.; Malekzadeh-Najafabadi, J.; Werner, J.P.F.; Klemm, U.; Tang, L.; Chen, Z.; Prakash, J.; Huang, Y.; Stiel, A.; et al. Croconaine-Based Nanoparticles Enable Efficient Optoacoustic Imaging of Murine Brain Tumors. *Photoacoustics* **2021**, *22*, 100263. [[CrossRef](#)] [[PubMed](#)]
71. Biyikloğlu, Z.; Bas, H.; Alp, H. Non-Aggregated Axially Disubstituted Silicon Phthalocyanines Bearing Electropolymerizable Ligands and Their Aggregation, Electropolymerization and Thermal Properties. *Dalton Trans.* **2015**, *44*, 14054–14062. [[CrossRef](#)] [[PubMed](#)]
72. Mbambisa, G.; Nyokong, T. Synthesis and Electrochemical Characterisation of a near Infrared Absorbing Oxo Vanadium(IV) Octapentylthio-Phthalocyanine. *Polyhedron* **2008**, *27*, 2799–2804. [[CrossRef](#)]
73. Christie, R.M. Colour and Constitution Relationships in Organic Pigments. Part 5: The Influence of Solvents, the Central Metal Atom and Substituents on the Electronic Spectra of Phthalocyanines. *Dye. Pigment.* **1995**, *27*, 35–43. [[CrossRef](#)]
74. Tian, M.; Zhang, Y.; Wada, T.; Sasabe, H. Syntheses of Novel Non-Aggregated Binuclear Phthalocyaninato Vanadyl Complexes Using a Palladium-Catalyzed Cross-Coupling Reaction. *Dye. Pigment.* **2003**, *58*, 135–143. [[CrossRef](#)]

75. Lee, J.-H.; Gomez, I.J.; Sitterle, V.B.; Meredith, J.C. Dye-Labeled Polystyrene Latex Microspheres Prepared via a Combined Swelling-Diffusion Technique. *J. Colloid Interface Sci.* **2011**, *363*, 137–144. [[CrossRef](#)] [[PubMed](#)]
76. Gvozdev, D.A.; Solovchenko, A.E.; Martynov, A.G.; Yagodin, A.V.; Strakhovskaya, M.G.; Gorbunova, Y.G.; Maksimov, E.G. Fluorescence Quenching of Carboxy-Substituted Phthalocyanines Conjugated with Nanoparticles under High Stoichiometric Ratios. *Photonics* **2022**, *9*, 668. [[CrossRef](#)]
77. Bush, P.G.; Wokosin, D.L.; Hall, A.C. Two-versus One Photon Excitation Laser Scanning Microscopy: Critical Importance of Excitation Wavelength. *Front. Biosci.* **2007**, *12*, 2646–2657. [[CrossRef](#)]
78. Dubinina, T.V.; Ivanov, A.V.; Borisova, N.E.; Trashin, S.A.; Gurskiy, S.I.; Tomilova, L.G.; Zefirov, N.S. Synthesis and Investigation of Spectral and Electrochemical Properties of Alkyl-Substituted Planar Binuclear Phthalocyanine Complexes Sharing a Common Naphthalene Ring. *Inorg. Chim. Acta* **2010**, *363*, 1869–1878. [[CrossRef](#)]
79. Song, C.J.; Jang, C.K.; Yao, W.; Jaung, J.Y. Synthesis and Spectral Characterisation of Dicyanopyrazine-Related Cyanoheterocycles. *J. Chem. Res.* **2013**, *37*, 268–272. [[CrossRef](#)]
80. Frisch, M.J.; Trucks, G.W.; Schlegel, H.B.; Scuseria, G.E.; Robb, M.A.; Cheeseman, J.R.; Scalmani, G.; Barone, V.; Mennucci, B.; Petersson, G.A. *Gaussian 09, Revision, D. 01, Programme*; Gaussian Inc.: Wallingford, CT, USA, 2009.
81. Tomasi, J.; Mennucci, B.; Cammi, R. Quantum Mechanical Continuum Solvation Models. *Chem. Rev.* **2005**, *105*, 2999–3094. [[CrossRef](#)]
82. Rappe, A.K.; Casewit, C.J.; Colwell, K.S.; Goddard, W.A.; Skiff, W.M. UFF, a Full Periodic Table Force Field for Molecular Mechanics and Molecular Dynamics Simulations. *J. Am. Chem. Soc.* **1992**, *114*, 10024–10035. [[CrossRef](#)]
83. Becke, A.D. Density-functional Thermochemistry. III. The Role of Exact Exchange. *J. Chem. Phys.* **1993**, *98*, 5648–5652. [[CrossRef](#)]
84. Grimme, S.; Ehrlich, S.; Goerigk, L. Effect of the Damping Function in Dispersion Corrected Density Functional Theory. *J. Comput. Chem.* **2011**, *32*, 1456–1465. [[CrossRef](#)] [[PubMed](#)]
85. Andrae, D.; Häußermann, U.; Dolg, M.; Stoll, H.; Preuß, H. Energy-Adjusted ab Initio Pseudopotentials for the Second and Third Row Transition Elements. *Theor. Chim. Acta* **1990**, *77*, 123–141. [[CrossRef](#)]
86. Dunning, T.H.; Hay, P.J. *Modern Theoretical Chemistry*; Plenum: New York, NY, USA, 1977; Volume 3, pp. 1–28.
87. Yanai, T.; Tew, D.P.; Handy, N.C. A New Hybrid Exchange–Correlation Functional Using the Coulomb-Attenuating Method (CAM-B3LYP). *Chem. Phys. Lett.* **2004**, *393*, 51–57. [[CrossRef](#)]
88. Adamo, C.; Barone, V. Toward Reliable Density Functional Methods without Adjustable Parameters: The PBE0 Model. *J. Chem. Phys.* **1999**, *110*, 6158–6170. [[CrossRef](#)]
89. Zhao, Y.; Truhlar, D.G. The M06 Suite of Density Functionals for Main Group Thermochemistry, Thermochemical Kinetics, Noncovalent Interactions, Excited States, and Transition Elements: Two New Functionals and Systematic Testing of Four M06-Class Functionals and 12 Other Function. *Theor. Chem. Acc.* **2008**, *120*, 215–241. [[CrossRef](#)]

Disclaimer/Publisher’s Note: The statements, opinions and data contained in all publications are solely those of the individual author(s) and contributor(s) and not of MDPI and/or the editor(s). MDPI and/or the editor(s) disclaim responsibility for any injury to people or property resulting from any ideas, methods, instructions or products referred to in the content.